The Astrophysical Journal, 589:844–860, 2003 June 1

NANOLENSING OF GAMMA-RAY BURSTS

Mark A. Walker[1,2,3] and Geraint F. Lewis[1,4]
Received 2002 December 15; accepted 2003 February 10

ABSTRACT

All quasars vary in their optical flux on a timescale of years, and it has been proposed that these variations are principally due to gravitational lensing by a cosmologically distributed population of planetary-mass objects. This interpretation has implications for the observable properties of gamma-ray bursts (GRBs)—as a source expands across the nanoarcsecond caustic network, variability is expected—and data on GRBs can be used to test the proposed model of quasar variability. Here we employ an ultrarelativistic blast wave model of the source, with no intrinsic variations, to study the effects of nanolensing on GRBs. Taken in isolation, the light curves of the caustic crossings are predictable, and we find that a subset of the predicted light curves (the image-annihilating fold crossings) resembles the "pulses" that are commonly seen in long GRBs. Furthermore, for sources at high redshift, the expected time between caustic crossings is of the order of seconds, comparable to the observed time between pulses. These points suggest that it might be possible to model some of the observed variations of GRBs in terms of nanolensing; however, our simulated light curves exhibit a small depth of modulation compared to what is observed. This means that the GRB data do not significantly constrain the quasar nanolensing model; it also means that the simplest nanolensing model cannot explain the observed GRB pulses. Viable nanolensing models for pulses probably require a large external beam shear. If a viable model can be constructed, it would effect a considerable simplification in source modeling and, ironically, it would explain why no macrolensed GRBs have been identified to date. Independent of the particular theoretical model, we can test for the presence of nanolensing in GRB data because any variability due to nanolensing should manifest parallax: the timing of caustic crossings, and hence the temporal substructure of bursts, should be different as seen by separated observers. Parallax therefore shifts triangulated burst locations away from their true positions; this displacement is typically expected to be at the few-arcminute level, and existing astrometry is not good enough to reveal the predicted effects. Useful constraints can, however, be obtained by comparing the relative timing of individual peaks in the light curves recorded by spacecraft in the Interplanetary Network; published data show hints of the predicted temporal shifts, but the photon counting statistics are not good enough to categorically decide the matter. There is no plausible alternative interpretation for this phenomenon, and if it is confirmed as a real effect then it compels acceptance of a cosmology that is very different from the currently popular model.

Subject headings: dark matter — gamma-ray bursts — gravitational lensing

1. INTRODUCTION

At present we do not know what constitutes the bulk of the material universe, i.e., the dark matter. Many dark matter candidates have been proposed, ranging from elementary particles to macroscopic objects such as black holes—see, e.g., Trimble (1987), Ashman (1992), and Carr (1994). To date it has been possible to eliminate some suggestions (e.g., brown dwarfs; Tinney 1999) by virtue of a clear conflict between models and data, but a positive identification has not been achieved. One proposal whose implications have not yet been thoroughly explored is that of Hawkins (1993, 1996), who argued, on the basis of photometric monitoring of quasars, that the universe contains a near-critical density of planetary-mass objects (see Press & Gunn 1973). Gravitational lensing by such a population is capable of explaining much of the observed variability (see also Schneider & Weiss 1987; Schneider 1993), although this should not be taken to imply that intrinsic variations are absent. This suggestion is a radical departure from the now-standard picture of a universe dominated by elementary particles (i.e., cold dark matter; see, e.g., Peebles 1993; Blumenthal et al. 1984; Davis et al. 1985) and has received little theoretical attention. Building on earlier work (Schneider & Wagoner 1987; Rauch 1991; Seljak & Holz 1999; Metcalf & Silk 1999), Minty, Heavens, & Hawkins (2001) described a statistical test of the model based on the light curves of distant supernovae, but existing data do not allow these ideas to be usefully implemented. A test based on surface brightness variability in low-redshift galaxies has been described by Lewis & Ibata (2001), but this idea also requires data that are not yet available, as does the test based on monitoring quasars seen through low-redshift clusters of galaxies (Walker & Ireland 1995; Tadros, Warren, & Hewett 1998). Data from the MACHO and EROS experiments exclude planetary-mass compact objects as a significant contributor to the Galactic dark matter (Alcock et al. 1998). However, objects that are sufficiently compact that they qualify as strong gravitational lenses at cosmological distances are not necessarily strong gravitational lenses when they are located in the Galactic halo (Walker 1999; see also Draine 1998; Rafikov & Draine 2001). The Galactic microlensing experiments therefore do not directly test the quasar nanolensing hypothesis.

[1] School of Physics, University of Sydney, A28, Sydney, NSW 2006, Australia.
[2] Australia Telescope National Facility, CSIRO, P.O. Box 76, Epping, NSW 2121, Australia.
[3] Raman Research Institute, CV Raman Avenue, Sadashivanagar PO, Bangalore 560-080, India.
[4] Anglo-Australian Observatory, P.O. Box 296, Epping, NSW 1710, Australia.

It is obvious that one could attempt to devise further, more sophisticated tests of the nanolensing interpretation based on existing quasar data, but it is a priori unlikely that any such test will yield a definitive result. The main reason for this is source size: the low amplitude of variations seen in quasar optical light curves means that these sources are necessarily larger than the scale size of the hypothesized caustic structure, thus smoothing the magnification pattern, and in the process destroying the high spatial frequency information. (This would be less of a barrier to progress if we had a reliable model for the physical structure of quasars, so that detailed predictions for their lensed appearance could be given with some confidence.) For example, the approach of Dalcanton et al. (1994; see also Canizares 1982), based on the statistics of equivalent widths of quasar emission lines, is quite insensitive in this regime in which the continuum source is resolved by the lenses. To make progress, we therefore require a numerous population of small, highly luminous sources at large distances; gamma-ray bursters constitute such a population. Gravitational lensing of gamma-ray bursts (GRBs) has previously been considered by a number of authors (e.g., Paczyński 1986b; McBreen & Metcalfe 1988; Mao 1992; Gould 1992; Blaes & Webster 1992; Nemiroff & Gould 1995), but their considerations are relevant to lenses that are either much more massive or much less massive than the planetary-mass range that we consider here. The present work also differs substantively from previous investigations in that the evolution (expansion) of the source structure plays a critical role in our analysis.

Following the launch of the *Compton Gamma-Ray Observatory*, BATSE (the Burst And Transient Source Experiment) soon discovered that GRBs are isotropically distributed on the sky and that they depart from Euclidean source counts at low flux levels (Fishman et al. 1994). These discoveries immediately shifted attention away from interpretations based on Galactic neutron stars, which had previously been popular, toward a variety of models in which energies amounting to a significant fraction of $M_\odot c^2$ are rapidly released by sources at cosmological distances (see Paczyński 1995). Discovery of X-ray afterglows from these transient events (Costa et al. 1997) by *BeppoSAX* allowed the sources to be accurately positioned and thus led to the discovery of optical and radio afterglows (van Paradijs et al. 1997; Djorgovski et al. 1997; Frail et al. 1997). Spectroscopy of these optical transients has in some cases revealed absorption lines from gas at redshifts $z_s \gtrsim 1$, thus firmly establishing the distance scale of the bursters to be cosmological (Metzger et al. 1997; van Paradijs, Kouveliotou, & Wijers 2000).

Although we still do not know what process injects the burst energy, it is broadly agreed that the radiation observed from GRBs arises from a relativistically expanding source. Relativistic expansion is required in order that we should see gamma rays at all—at least at energies $\gtrsim$ MeV—otherwise the inferred source size is so small, and the photon energy density so high, that two-photon pair production converts essentially all the gammas into material particles (Cavallo & Rees 1978; Fenimore, Epstein, & Ho 1993; Baring & Harding 1997). These considerations require expansion with Lorentz factors of at least $\Gamma \sim 10^2$.

At an early stage in the modeling of GRBs in a cosmological context, it was pointed out that gamma-ray emission should arise as the ambient medium undergoes shock compression by the expanding material (Rees & Mészáros 1992). This picture—the "blast wave" or "external shock" model—now provides the accepted context for modeling the broadband (X-ray, optical, and radio) afterglows of bursts (Paczyński & Rhoads 1993; Mészáros & Rees 1997; Granot, Piran, & Sari 1999) but has fallen into disfavor as an interpretation of the prompt GRB. The reason for the demise of this model is simply that it cannot, in itself, accommodate the rapid, large-amplitude variability that is manifest in the gamma-ray data (Fenimore, Madras, & Nayashkin 1996; Sari & Piran 1997; see also Dermer & Mitman 1999; Fenimore, Ramirez-Ruiz, & Wu 1999). This point has promoted the idea that the gamma rays arise from internal shocks within the relativistic outflow, so that the temporal variations of the burst reflect the input power variations of the source (see, e.g., Rees & Mészáros 1994; Kobayashi, Piran, & Sari 1997).

Because we are investigating an hypothesis in which apparent variability arises external to the source, as a result of gravitational lensing, arguments that assume that the observed variations are intrinsic immediately lose most, if not all, of their force. Given this, there are at least three motivations to return to the blast wave interpretation of the prompt gamma-ray emission: first, this picture allows the initial deposition of energy to be impulsive and is therefore suitable for a broad range of source models (independent of the specific physics of the energy input) with no fine-tuning required; second, the low radiative efficiency of internal shocks (Spada, Panaitescu, & Mészáros 2000) appears to be inconsistent with the event energetics in at least some cases (Paczyński 2001); and third, gamma-ray emission from an external shock ought to be present at some level. This emission can be sensibly described by a self-similar, decelerating blast wave model, similar to those developed for the afterglow emission (see, e.g., Granot et al. 1999), but radiative rather than adiabatic. Such a description leads us to expect a circular source with *very* strong limb brightening, and consequently, we anticipate significant flux variations if the limb crosses a caustic. This thin, bright, and rapidly expanding ring is a near-perfect instrument for revealing any caustic structure that might be present along the line of sight to the source—see also Loeb & Perna (1998) and Mao & Loeb (2001), who considered microlensing of optical afterglows by stellar-mass objects in the low optical depth limit.

In this paper we use the source model just described to explore the hypothesis that the universe contains a high density of planetary-mass objects, with an optical depth to gravitational lensing of the order of unity. Often the characteristic angular scale of the lenses (in arcseconds) is indicated in the nomenclature given to associated phenomena (e.g., *microlensing*), and, following this convention, dictates the name "nanolensing" for the effects discussed herein. Although gravitational lensing is the main focus of our attention here, in studying the variations that might be introduced by this process, we are also implicitly addressing the physics of the sources themselves. We start by presenting our source model in § 2, and in § 3 we turn to aspects of the gravitational lensing; light curves that result from the marriage of these elements are presented and compared with data in § 4. The role of parallax is explored in § 5, followed by a discussion of related issues concerning both the lenses and the sources (§ 6), and our conclusions are given in § 7.

2. SOURCE MODEL

Following Rees & Mészáros (1992), we adopt a spherically symmetric, ultrarelativistic blast wave model of the GRB phenomenon, in which a total energy of $10^{52}\,E_{52}$ ergs resides in ejecta that expand with an initial Lorentz factor $\gamma = 10^3\gamma_3 \gtrsim 10^3$ into a homogeneous medium of density n cm^{-3}. At first the ejecta coast ($\gamma \simeq$ constant), but this lasts only for a brief period, $\sim 0.1\gamma_3^{-8/3}(E_{52}/n)^{1/3}$ s, and subsequently the ejecta decelerate, with some fraction of the thermalized power appearing as radiation. We will treat these as distinct, self-similar phases of evolution, characterized by the index m, where

$$\Gamma^2 = \Gamma_0^2\left(\frac{R_0}{R}\right)^m \tag{1}$$

at radius R and $\Gamma = \sqrt{2}\gamma$ is the Lorentz factor of the shock wave that precedes the ejecta (Blandford & McKee 1976). In the coasting phase we evidently have $m = 0$, while $m = 3$ for adiabatic evolution and $m = 12$ for a fully radiative blast wave—i.e., one in which all of the thermalized energy is promptly radiated away (Cohen, Piran, & Sari 1998). The adiabatic approximation is appropriate for the afterglow, when the radiation timescale is much longer than the expansion timescale; for the GRB itself, we adopt the fully radiative solution, $m = 12$. In this circumstance the gamma rays arise from a thin shell immediately behind the shock front.

It is convenient to take R_0 as the radius at which the transition between coasting and semiradiative solutions takes place and to model the evolution of the blast wave as if there were an instantaneous transition between these solutions, as the shock crosses this radius. We can estimate the value of R_0 by noting that the shock will start to decelerate when a significant fraction of the initial energy of the blast has been thermalized (Rees & Mészáros 1992):

$$R_0 \simeq 1.2\times 10^{16}\left(\frac{E_{52}}{n\Gamma_3^2}\right)^{1/3}\ \text{cm}\ . \tag{2}$$

Where numerical estimates are required we adopt the values $E_{52} = \Gamma_3 = n = 1$ throughout. For some estimates, we need to know, in addition, the Hubble constant, which we take to be $H_0 = 70\,\text{km s}^{-1}\,\text{Mpc}^{-1}$.

In this paper we consider only bolometric radiation properties, so that it is not necessary to specify the radiation mechanism.

2.1. *Kinematics*

Because the expansion is spherically symmetric, the observed source structure is axisymmetric, and at any given time it can be expressed as a function of a single variable, such as the apparent radius r, as measured by a distant observer, relative to the line of sight to $R = 0$. Because the expansion is relativistic, it is essential to incorporate light-travel time in any computation of the appearance of the source. In terms of the time t, measured by a distant observer *at the same redshift* (with $t = 0$ corresponding to the start of the expansion), there is a maximum apparent radius $r_{\max}$ from which photons can be received by the observer,

$$r_{\max}^{2m+2} = \Gamma_0^2 R_0^m\left[\left(\frac{2m+2}{m+2}\right)ct\right]^{m+2}\ , \tag{3}$$

and this defines the limb of the source at any time. In general, we expect the source to be at nonzero redshift z_s, and to allow for this, one simply makes the replacement $t \to t/(1+z_s)$, both here and in subsequent formulae. In cases in which a numerical estimate is required, we adopt the value $z_s = 5$ throughout this paper; this corresponds to the median redshift in the GRB source population model of Bromm & Loeb (2002). The radius at $r = r_{\max}$ is given by $R_{\max}$:

$$R_{\max}^{m+1} = 2ct\Gamma_0^2 R_0^m\left(\frac{m+1}{m+2}\right)\ , \tag{4}$$

and if we define $q \equiv R/R_{\max}$, then for any point on the emitting surface, at any given time, we have

$$\tilde{r}^2 = \frac{q}{m+1}\left[(m+2) - q^{m+1}\right]\ , \tag{5}$$

where $\tilde{r} \equiv r/r_{\max}$. Notice that there are two values of q that correspond to each value of $\tilde{r}$ (other than $\tilde{r} = 1$); one of these values lies in the range $0 \le q < 1$, while the other lies in the range $1 < q \le Q$, with $Q^{m+1} = m+2$.

Knowing the apparent size of the source as a function of time, we can easily find the apparent expansion speed $\beta_{\rm ap}$ (in units of c) just by differentiating equation (3):

$$\beta_{\rm ap}^{2m+2} = \Gamma_0^2\left[\frac{(m+2)R_0}{(2m+2)ct}\right]^m\ . \tag{6}$$

2.2. *Intensity Profile*

By virtue of being almost coincident with the shock front, the emitting surface exhibits the geometry of a shell moving with Lorentz factor Γ, as described in § 2.1. However, the emitting particles are part of the postshock flow, so their bulk Lorentz factor is $\gamma = \Gamma/\sqrt{2}$, and in consequence the limb of the source ($\tilde{r} = 1$) does not correspond to the peak of the observed intensity. This point does not appear to have been recognized previously (cf. Granot & Loeb 2001; Gaudi, Granot, & Loeb 2001). For a thin emitting shell, the peak surface brightness corresponds to polar angle $\psi = \pi/2$ (as measured in the comoving frame) relative to the surface normal. For an emitting shell of fractional radial thickness $\Delta \ll 1$, the bolometric surface brightness can be described by

$$I(r,\,t) = \frac{\mathscr{D}^4\mathscr{I}}{\sqrt{\cos^2\psi + \Delta/4}}\ , \tag{7}$$

with $\mathscr{I}$ being the bolometric intensity emitted normal to the surface, as measured in the rest frame of the emitting shell, and $\mathscr{D}$ the Doppler factor. [Recall that $q(\tilde{r})$ is double-valued, so that there are implicitly two contributions to the right-hand side of eq. (7).] It is easy to show that rays reaching the observer at a given instant satisfy

$$\cos\psi = \frac{(2m+3)q^{m+1} - (m+2)}{(2m+1)q^{m+1} + (m+2)} \tag{8}$$

and that the ratio of observed to emitted photon energies is

$$\mathscr{D} = \frac{4(m+1)\gamma_{\max}q^{(m+2)/2}}{(2m+1)q^{m+1} + (m+2)}\ , \tag{9}$$

where $\gamma_{\max}\sqrt{2} := \Gamma_0(R_0/R_{\max})^{m/2}$. Now the total energy density in the postshock gas is just $4\gamma^2 nm_pc^2$ (Blandford &

McKee 1976), and in the frame of this material the shock itself moves at speed $c/3$, so if all of this power is promptly radiated, the emergent normal intensity (i.e., at $\psi = 0$) is

$$\mathscr{I} \simeq \frac{1}{3\pi}\gamma^2 n m_p c^3 \ . \tag{10}$$

The above set of equations provides a complete prescription for calculation of the bolometric intensity profile; the fully radiative case, corresponding to $m = 12$, is shown in Figure 1 for a fractional shell thickness of $\Delta = 4 \times 10^{-3}$. This choice for Δ is appropriate to, for example, synchrotron emission at $\sim$200 keV if the magnetic field energy density is 10% of the equipartition value. The essential feature of this profile is that it is *very* strongly limb-brightened, with a sharp peak at $r \simeq 0.99295 r_{\max}$ [corresponding to $q^{m+1} := (m+2)/(2m+3)$, i.e., $\psi = \pi/2$]. Source intensity profiles for any index $3 \le m \le 12$ exhibit this limb-brightening effect, but as m increases the limb-to-center intensity ratio grows according to $(32/27)(m+2)^{3m/(m+1)}$, and the peak-to-center intensity ratio equals $(2m+3)^{3m/(m+1)}/8\sqrt{\Delta}$; the peak also shifts to larger radii with increasing m.

The received flux is computed in the usual way, i.e.,

$$F = \int d\Omega\, I \propto 2\pi r_{\max}^2 \int_0^1 d\tilde{r}\,\tilde{r} I \ . \tag{11}$$

Using equation (5) it is straightforward to rewrite the integral over $\tilde{r}$ as an integral over q such that $0 \le q \le Q$. In this way we find that the observed flux should vary as $F \propto t^{(2-m)/(m+1)}$, so that F grows as t^2 during the early, coasting phase ($m = 0$) and then declines as $t^{-10/13}$ during the self-similar radiative ($m = 12$) evolution. A simple model light curve can thus be constructed by applying these two solutions in their appropriate regimes (small and large t, respectively) and switching between the two at the point where they cross. That is the procedure we shall follow here—our calculations are intended to be illustrative, and high precision is not needed. One important point to note is that the luminosity in the self-similar deceleration phase declines too slowly to yield a finite radiated energy at late times, and so the model clearly has a limited range of applicability.

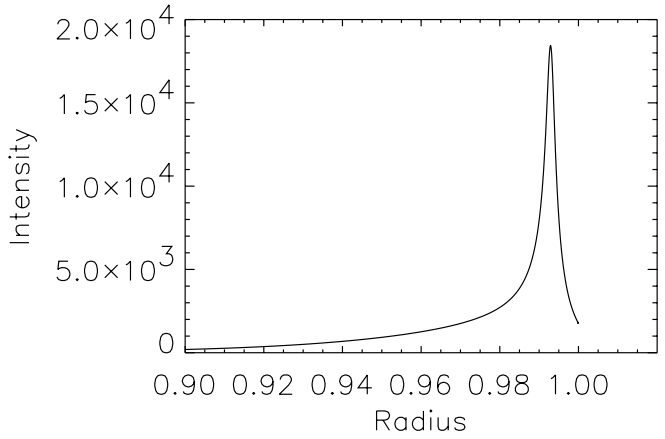

FIG. 1.—Radial distribution of bolometric intensity for a blast wave in self-similar, fully radiative ($m = 12$) evolution. The emitting shell is assumed to have a fractional radial thickness $\Delta = 4 \times 10^{-3}$. The intensity is normalized to the central intensity and declines monotonically beyond the left-hand edge of the plot. The location of the peak ($\tilde{r} \simeq 0.993$) corresponds to $\psi = \pi/2$, i.e., tangent to the emitting shell.

3. LENS MODEL

If the universe contains a mean mass density in lenses $\Omega_{\rm lens}$ (in units of the critical density), then the optical depth to gravitational lensing is $\tau \simeq 0.11\Omega_{\rm lens}$ for a source at redshift $z_s = 1$ and $\tau \simeq 0.62\Omega_{\rm lens}$ for a source at redshift $z_s = 5$ (Turner, Ostriker, & Gott 1984). These results are for a universe with a mean total density of $\Omega = 1$ (the cosmological constant, $\Lambda = 0$), and for a given redshift, the ratio $\tau/\Omega_{\rm lens}$ increases as Ω decreases. The study by Schneider (1993) demonstrated that $\Omega_{\rm lens} \sim 0.5$ is required (see his Fig. 6*b*) if the variability reported by Hawkins (1993) is attributed to gravitational lensing. The nanolensing interpretation of quasar variability is also consistent with the currently favored combination of cosmological model parameters ($\Lambda \simeq 0.7$, $\Omega \simeq 0.3$), provided that essentially all of the matter is in the form of lenses, i.e., $\Omega_{\rm lens} \simeq 0.3$ (Minty 2001). The details of the cosmological model are unimportant here; for simplicity of calculation, we have therefore adopted a model universe with $\Omega_{\rm lens} = \Omega = 1$.

The magnification pattern that is introduced by the lenses takes the form of a caustic network in which the appearance of any source is influenced by a large number of lenses (Paczyński 1986a); an example of such a network is shown in Figure 2. In this figure we see a large number of fold caustics—a fold is the lowest order catastrophe at which two images merge—joined by cusps (catastrophes where three images merge). In the present paper we illustrate the effects of GRB nanolensing through analytic and numerical calculations of a source crossing a single fold caustic (this section). We then (§ 4) simulate the global light curves expected for a source expanding across a caustic network such as that shown in Figure 2.

In the immediate vicinity of a fold caustic the mapping between rectangular source coordinates (x, y) and image coordinates (X, Y) is well approximated by a quadratic form (see Schneider, Ehlers, & Falco 1992):

$$x = \tfrac{1}{2} a X^2 \ , \qquad y = 2Y \ , \tag{12}$$

with the x-axis oriented perpendicular to the caustic and the curvature a being a positive constant. Here the factor $\frac{1}{2}$ in the $x \leftrightarrow X$ mapping is arbitrary (because a remains unspecified), but the factor of 2 in the $y \leftrightarrow Y$ mapping is required in order that the fold be convergence-free—a pure shear lens mapping—as all empty-beam lens mappings must be in general relativity. There are two solutions (images) to these equations for any source located at $x > 0$, and it is straightforward to determine their magnifications:

$$\mu_\pm = \pm \frac{1}{2\sqrt{2ax}} \ . \tag{13}$$

In addition to this image pair, there will typically be a large number of other images present, but the observed flux variations around the time of caustic crossing are completely dominated by the two very bright images that are described by equations (12) and (13). If a burst occurs at any location $x < 0$, then neither of these two images will be present until the source expands so as to touch the caustic, at which point the observed flux will rise abruptly. On the other hand, if a

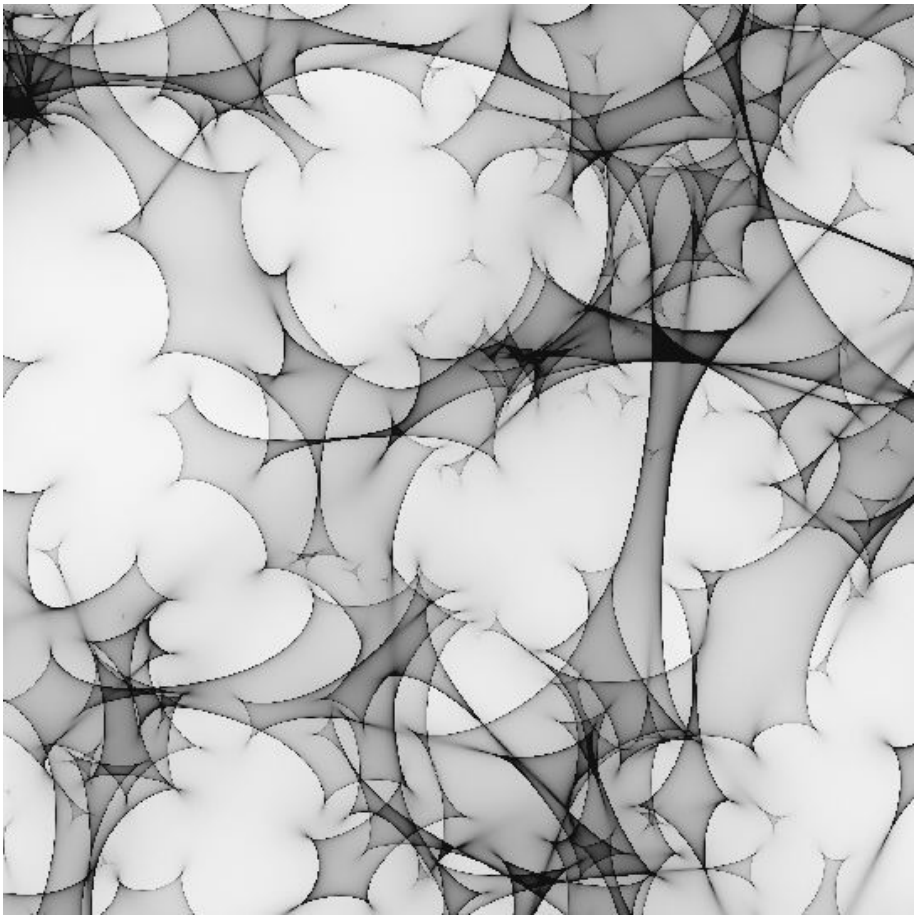

FIG. 2.—One realization of a magnification pattern appropriate to a source at redshift $z_s = 5$, in a universe populated with point mass lenses such that $\Omega_{\rm lens} = \Omega = 1$. This pattern is derived from a simulation in which the locations of the lenses are chosen randomly within a single plane, having a total optical depth of 0.6. The rays are chosen to have a uniform density across the image plane; this figure shows their density across the source plane; regions of high ray density in this figure are therefore areas of high magnification, and most of these regions correspond to fold caustics. Our simulations utilized code from Wambsganss et al. (1990).

burst occurs at $x > 0$, then both images will be present at all times.

There are two separate cases that we must consider, depending on which side of the caustic the burst occurs. For a point source at $x < 0$, there are $2n + 1$ images, whereas for $x > 0$, there are $2n + 3$; we therefore denote these two regions as the one-image and three-image regions, respectively, with the understanding that there are many more images present, but only the pair created/annihilated at $X = 0$ is of interest here. If the source takes the form of a thin ring, as is approximately the case for the model we have adopted (§ 2; see Fig. 1), then the lensed images appear as shown in Figure 3. In our subsequent development we denote the x-coordinate of the origin of the burst by s, so that the sign of s determines whether one or three images are initially present.

3.1. *Burst in Single-Image Region* ($s < 0$)

Because the source intensity distribution is axisymmetric, it is useful to consider the properties of an infinitesimally thin ring, radius r, of uniform surface brightness, under the mapping given by equation (12). If the burst occurs at $s < 0$, then images of the source first appear when the source reaches a radius $r = |s|$, and for $r > |s|$, the total magnification of the ring (summed over both images) is given by

$$\mu_1 = \frac{1}{\pi}\sqrt{\frac{u}{ar}}\mathscr{F}(\phi|u)\ , \tag{14}$$

where $\mathscr{F}$ denotes the incomplete elliptic integral of the first kind: $\cos 2\phi := -s/r$ and $u \equiv 2r/(r + s)$. Here "magnification" means the total area occupied by the two images of the annulus, divided by the area of the annulus itself. Simple approximations to this exact result are available: $\mu_1 \simeq (1 - 3\epsilon/8)/2(a|s|)^{1/2}$ for $0 < \epsilon \ll 1$, where $\epsilon \equiv r/|s| - 1$, and $\mu_1 \to \mathscr{K}(1/2)/\pi(ar)^{1/2}$ for $r \to \infty$, where $\mathscr{K}$ is the complete elliptic integral of the first kind and $\mathscr{K}(1/2) \simeq 1.8541$. The exact form of the magnification, given by equation (14), is graphed in Figure 4 for the case $s = -1/a$.

3.2. *Burst in Three-Image Region* ($s > 0$)

For a burst that occurs in the three-image region ($s > 0$), the total magnification of an annulus is given by

$$\mu_3 = \frac{1}{\pi}\sqrt{\frac{u}{ar}}\mathscr{K}(u) \tag{15}$$

for $r < s$. On the other hand, for $r > s$, we have (as with

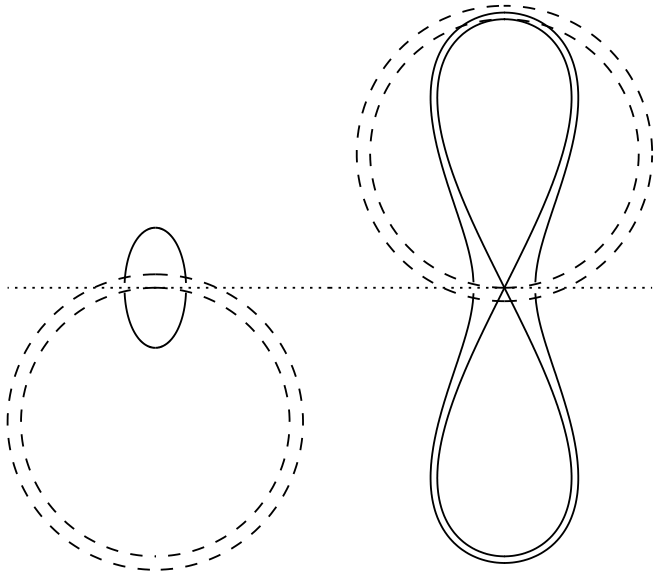

FIG. 3.—Images (*solid lines*) of two thin (10% fractional width), annular sources (*dashed curves*), on either side of a fold caustic (*dotted line*). For convenience, the critical curve ($X = 0$) has been superimposed on the caustic ($x = 0$). The upper half of this figure is the three-image region, and the lower half is the single-image region. In each case the inner boundary of the annulus just touches the caustic, and the center of each source is assumed to lie at a distance of $s = \pm 1/a$ from the fold.

eq. [14])

$$\mu_3 = \frac{1}{\pi}\sqrt{\frac{u}{ar}}\,\mathscr{F}(\phi|u)\ . \tag{16}$$

Simple approximations can be found for these expressions in the following regimes: $\mu_3 \simeq 1/(2as)^{1/2}$ for $r \ll s$; $\mu_3 \simeq \ln(32/|\epsilon|)/2\pi(as)^{1/2}$, where $|\epsilon| \ll 1$ (and $\epsilon = r/s - 1$); and $\mu_3 \simeq \mathscr{K}(1/2)/\pi(ar)^{1/2}$ for $r \to \infty$. The exact results are shown in Figure 4, for the case in which $s = 1/a$, alongside

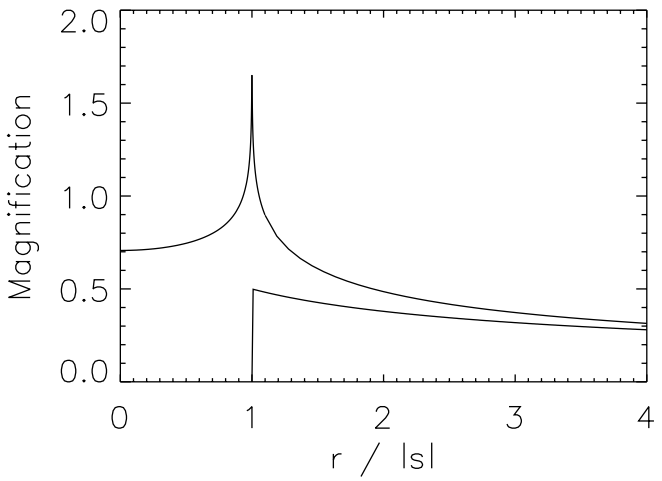

FIG. 4.—Magnification of an infinitesimally thin, annular source, of radius r, centered on $x = s$, under the mapping given in eq. (12); this mapping describes a pure shear fold caustic at $x = 0$. Here we have assumed that the curvature of the lens mapping near the fold is $a := 1/|s|$. The upper curve corresponds to $s > 0$ (burst occurs in three-image region), and the lower curve corresponds to $s < 0$ (burst in single-image region).

the corresponding magnification curve for a burst occurring in the single-image region.

3.3. *The Median Lens*

For some purposes (e.g., estimating a characteristic length scale in the source plane), it is important to know whereabouts on the line of sight the typical lens is located. This need is most sensibly addressed by determining the redshift at which the optical depth to gravitational lensing is one-half of the total optical depth for the source under consideration. Using equation (2.13b) of Turner et al. (1984), this can be quite straightforwardly achieved, and the result is that for a source at redshift z_s, the median lens is located at redshift $\langle z\rangle$:

$$\langle 1 + z\rangle = \sqrt{1 + z_s}\ . \tag{17}$$

Thus, for a source at redshift $z_s = 3$, the median lens redshift is unity, and at low redshift ($z_s \ll 1$) the median lens is located half-way to the source.

One application of the foregoing is the relationship between transverse dimensions measured in the source plane and in the observer's plane. Appropriate angular diameter distances for our circumstance are evidently "empty-beam" distances (for $\Omega = 1$), and these are given in Table 1 of Turner et al. (1984). Denoting observer-lens and lens-source angular diameter distances by D_d and D_{ds}, respectively, we introduce the "lever arm," $\varpi \equiv D_{ds}/D_d$. It is this ratio that, for any given lens, determines the relationship of a transverse distance in the source plane to the corresponding distance in the observer's plane. It is straightforward to show that the median lever arm (i.e., the lever arm of the median lens) is

$$\langle\varpi\rangle = (1 + z_s)^{-3/4}\ , \tag{18}$$

and we will make use of this result in § 5.

3.4. *Variability Timescale*

In combination with our kinematic model of the source structure (§ 2.1), the statistical properties of the caustic network determine the predicted variability timescale of GRBs as a function of source redshift and lens mass. At each occasion when the limb of the source crosses a caustic, a peak is introduced into the light curve, so the characteristic timescale between peaks is just the time taken by the source to expand in area by $1/\Sigma$, where Σ is the number of caustics per unit area in the source plane. In the low optical depth regime there are four folds in each projected Einstein ring. At high optical depth, where a caustic network develops, the caustic density is higher by a factor equal to the mean magnification, $(1 - \tau)^{-2}$, and we therefore estimate the caustic density by $\Sigma \sim 4\tau/(1 - \tau)^2$ per unit Einstein ring area in the source plane. The circumstance $\tau = 1$ corresponds to $z_s \simeq 10.7$ in our model universe, and the caustic density becomes very large, and the variability timescale correspondingly short, for sources around this redshift.

Using our self-similar ($m = 12$) source model, we can now estimate the expected variability timescale $t_{\rm var}$ via

$$t_{\rm var}^{-1} \sim \Sigma\frac{d}{dt}\pi r_{\rm max}^2\ . \tag{19}$$

It is worth noting that $r_{\rm max}^2 \propto t^{(m+2)/(m+1)}$ (see eq. [3]), so that the apparent area of the source increases nearly linearly

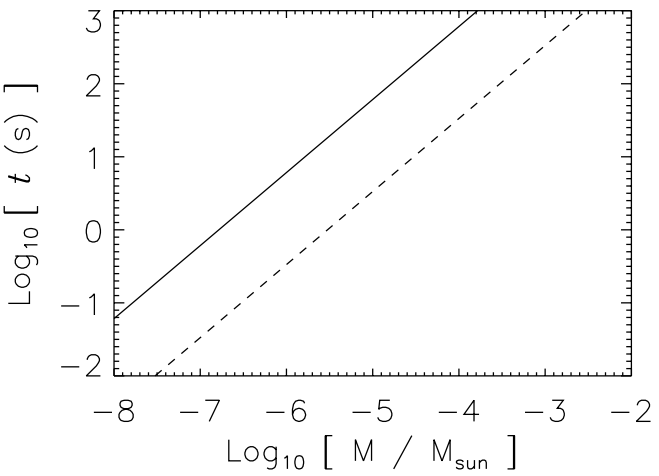

FIG. 5.—Nanolensing variability timescale, in a universe with $\Omega_{\rm lens} = \Omega = 1$, as a function of lens mass. The source is assumed to be in self-similar, fully radiative ($m = 12$) evolution with initial Lorentz factor $\Gamma_0 = 10^3$; other parameters characterizing the expansion have been fixed at $E_{52} = 1$ and $n = 1$. The solid line corresponds to a source at redshift $z_s = 1$, while the dashed line corresponds to a source at redshift $z_s = 5$.

with time, and the variability timescale is thus not expected to evolve significantly during a burst. The results are shown in Figure 5 as a function of lens mass, for two different values of the source redshift ($z_s = 1$, 5), and an initial Lorentz factor $\Gamma_0 = 10^3$. Considering that bursts may last up to several hundred seconds and that the available temporal resolution is below 100 ms in existing data, almost the entire temporal range in Figure 5 is open to study. We thus recognize that *a cosmological population of planetary-mass lenses should introduce variability to GRB profiles,* suggesting a powerful test of the nanolensing interpretation of quasar variability.

The model does not make a precise prediction for the time interval between caustic crossings because the appropriate lens mass is not tightly constrained (nor indeed are the parameters of the source, such as Γ_0). Hawkins (1993) initially gave an estimate of $10^{-3}\ M_\odot$, but Schneider's (1993) analysis clearly favors $10^{-4}\ M_\odot$ or even smaller values. Using three-dimensional ray-shooting simulations, Minty (2001) finds that these data suggest lens masses of 10^{-5} to $10^{-4}\ M_\odot$. Schild (1996) also suggests lens masses of $10^{-5} M_\odot$ in a relaxed context, namely, the variability of the individual images of a multiply imaged, macrolensed quasar. Referring to Figure 5, if we adopt $\Gamma_0 = 10^3$ and lens masses of the order of $10^{-5}\ M_\odot$, then the variability timescale is expected to be $\sim$60 s for a source at redshift $z_s \simeq 1$ and $\sim$4 s for a source at $z_s \simeq 5$.

4. LIGHT CURVES

We have taken two distinct approaches to the study of lensed light curves: detailed calculation of the behavior around the time of a fold caustic crossing event, exhibiting the type of profiles that are expected for individual "pulses" (Norris et al. 1996, hereafter N96), and simulation of light curves for GRBs seen through a caustic network. For any given burst, the latter reflects the random structure of the caustic network in the vicinity of the source. We note here that the propagation times for the various images in our model differ only by amounts $\lesssim 1$ ns, and this is negligible for our purposes.

4.1. *Individual "Pulses"*

Making use of the source intensity profile computed in § 2 and the magnification curves derived in the previous section, it is now a straightforward exercise to compute the flux history $F(t)$ from

$$F(t) \propto \int dr\, 2\pi r I(r, t)\mu\ , \tag{20}$$

where the total magnification μ can be written as the sum of the "unlensed" images (actually, a large number of lensed images whose total flux is roughly constant over the timescale of the caustic crossing) plus the bright pair of images associated with the fold caustic under consideration: $\mu = 1 + \mu_{1,3}$. (The choice of unity for the constant term in this relation is somewhat arbitrary.) As with equation (11), this formula can easily be rewritten as an integral over the variable q. After substituting for $I(r, t)$ (eqs. [7]–[10]) and $\mu_{1,3}$ (eqs. [14]–[16]) it is straightforward to evaluate equation (20) numerically; to do this, we used the Mathematica software package. The results are shown in Figure 6, for bursts occurring in both one- and three-image regions. For these calculations, we have assumed $|s| = 1/a$, and we have taken the fractional radial thickness of the emitting shell to be $\Delta = 4 \times 10^{-3}$. For each light curve, the limb of the source first touches the caustic at $t = 1.5$ s (an arbitrary choice).

Some aspects of Figure 6 require immediate comment. The difference in overall normalization of the two curves at early times simply reflects the ratio of total magnifications at the onset of the burst—see Figure 4—roughly $(1 + 1/\sqrt{2})/(1 + 0) \simeq 1.7$. This property is a direct result of the simple lens model we have adopted (i.e., the quadratic relationship between source and image coordinates), and it should be remembered that this approximation is accurate only in the immediate vicinity of the caustic. Consequently, it is the behavior seen in the light curves around $t = 1.5$ s that is of prime interest rather than the global properties. The essential features to note are, therefore, that (1) the

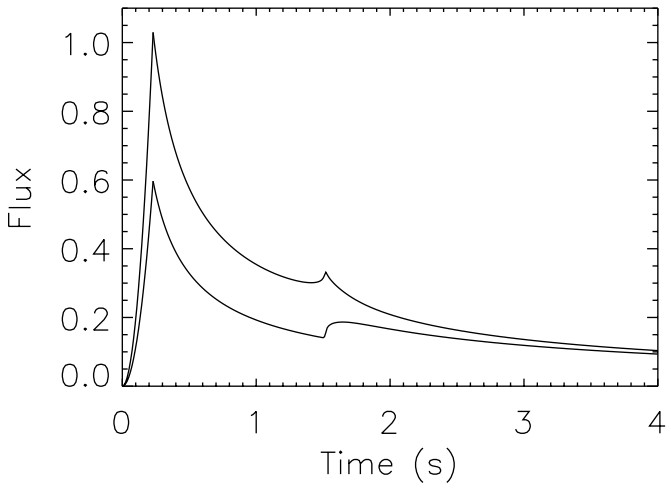

FIG. 6.—Bolometric gamma-ray light curves for a relativistic, fully radiative ($m = 12$), self-similar blast wave seen expanding across a fold caustic. The thickness of the radiating shell is taken to be $\Delta = 4 \times 10^{-3}$, and the center of expansion of the burst is assumed to be a distance $1/a$ from the fold, where a is the curvature of the lens mapping. The upper curve corresponds to a burst in the three-image region, while the lower curve is for an event in the single-image region; caustic crossing occurs at $t \simeq 1.5$ s.

presence of a fold caustic introduces a significant peak into the light curve, close to the time at which the limb of the source first touches the caustic, and (2) this peak can be either cuspy, and approximately time-symmetric, or rounded and asymmetric. These features could, in fact, have been anticipated simply by examining the magnification profiles shown in Figure 4, bearing in mind that the source structure is basically just a thin ring (Fig. 1).

4.2. *Simulated Light Curves*

Although the circumstance we are considering is one in which a population of gravitational lenses is distributed along the entire line of sight, we have made use of simulations that are two-dimensional, with all of the lenses located in a single plane. This is partly because three-dimensional ray-tracing simulations are much slower than their two-dimensional counterparts, but mainly because a well-tested two-dimensional code was available to us (Wambsganss, Paczyński, & Katz 1990). Two extensions of this code were required for our purposes: convolution of the magnification map with our model source intensity profile (§ 2) and a progressive "zoom" that recomputes the magnification map on larger scales as the source expands. The latter feature was implemented with an incremental zoom factor of 1.2, and our computational grid was 2048 pixels on a side, so that our source radius was in the range 800–1000 pixels. Despite this, our resolution is only just adequate for the task, as the reader can easily verify by examining the radial width of the source intensity distribution (Fig. 1). An estimate of the FWHM of the source intensity peak can be obtained from

$$\mathrm{FWHM} \simeq \left(\frac{m+2}{2m+3}\right)^{(m+2)/(m+1)} \frac{2\sqrt{3\Delta}}{2m+3}\ , \qquad (21)$$

and for $m = 12$ and $\Delta = 4 \times 10^{-3}$, this yields (coincidentally) FWHM $\simeq 4 \times 10^{-3}$. With a source radius of 800 pixels the intensity profile is thus 1.5 times oversampled.

To illustrate the type of light curve that might be expected, we have undertaken simulations for sources at redshift $z_s = 1$ and 5, corresponding to optical depths to gravitational nanolensing of $\tau = 0.11$ and 0.62, respectively. The results of these simulations are shown in Figures 7 and 8, for lenses of mass 10^{-8} and 10^{-5} $M_\odot$, respectively. Because the source evolves in a self-similar (scale-free) manner, it is not necessary to recompute magnification curves when the adopted lens mass is changed: different lens masses simply require a rescaling of the time axis in panel *a* of these figures, thus changing the characteristic timescale of any variability, but not its amplitude. The choice of lens mass was made, for each of the two redshifts, so as to maximize the variability within each of the synthetic bursts.

All of our simulations follow the same basic pattern: starting from an initial magnification that is below unity, the mean magnification (i.e., average magnification over the whole source) exhibits rapid variability, the amplitude of which decreases as the source expands. These features are readily understood. Initially, the source is likely to be demagnified because most of the area of the source plane is occupied by regions with magnification below unity. Subsequently, as the source expands across the caustics, variability is seen. However, accompanying the increase in source radius is an increase in the thickness of the high-intensity ring, and the modulation of the mean magnification of the source is consequently reduced. Simultaneously, the time-averaged magnification trends toward its large-scale average value as the source covers an increasing area.

There are two important points that are evident on examining Figures 7 and 8. First, the timescale of the variations in the simulated light curves is in broad agreement with the rough estimates given in § 3.4 (see Fig. 5). Second, the depth of modulation seen in our simulated magnification curves is quite small, being typically of the order of 10%, and in the light curves themselves, where the secular evolution is strong, it is not always apparent that the flux is varying on short timescales.

4.3. *Comparison with Observations*

Many high-quality GRB light curves were acquired by BATSE on the *Compton Gamma-Ray Observatory* (see, e.g., Fishman et al. 1994), and the substructure within these light curves has been analyzed by N96, in the case of long, bright bursts. The principal conclusion of this analysis was that

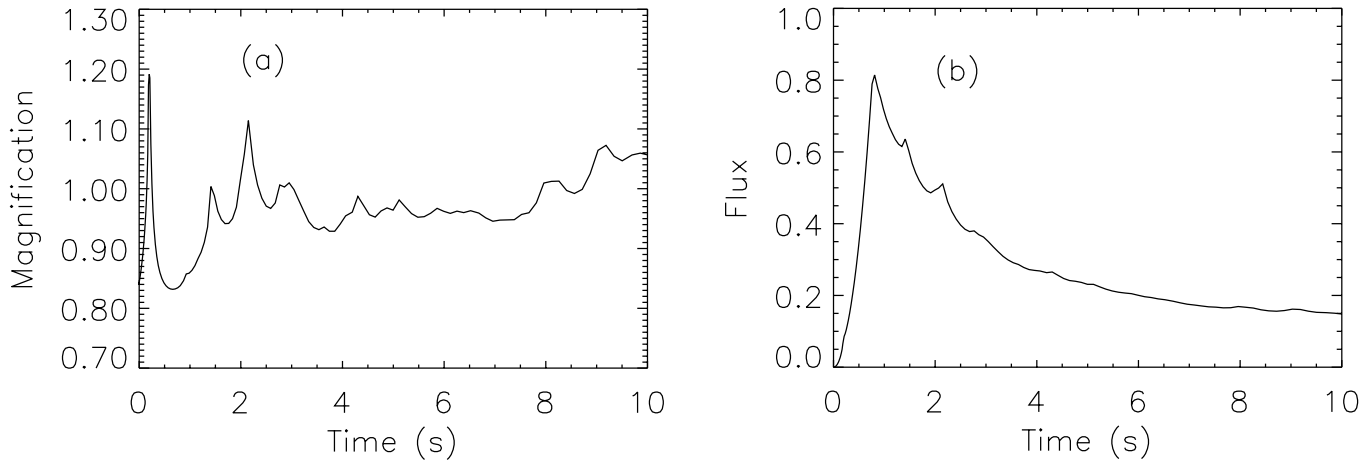

FIG. 7.—Simulations of (*a*) the mean magnification and (*b*) the resulting light curve for a GRB occurring at redshift $z_s = 1$, in a universe full of nanolenses ($\Omega = \Omega_{\rm lens} = 1$); each lens is assumed to have a mass of 10^{-8} $M_\odot$. The apparent timescale of the transition between coasting and radiative phases is given by $(1 + z_s)R_0/c\Gamma_0^2$, and for our adopted burst parameters ($E_{52} = n = \Gamma_3 = 1$), this corresponds to $0.39(1 + z_s)s$. This timescale defines the location of the peak of the burst in (*b*). Note that the magnification is in units of the theoretical average, $\langle \mu_{\rm th} \rangle = (1 - \tau)^{-2}$, which, for this case, is 1.26.

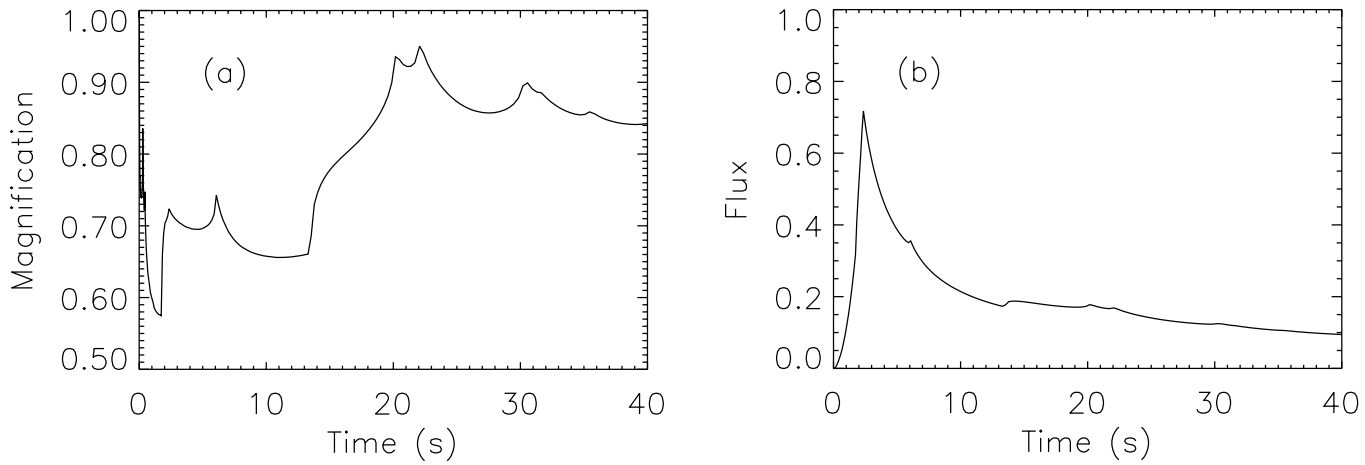

FIG. 8.—Same as Fig. 7, but for a source redshift of $z_s = 5$ (corresponding to the burst peak at $t = 2.3$ s) and lenses of mass $10^{-5}\ M_\odot$. Again, the magnification is in units of the theoretical average, $\langle \mu_{\rm th} \rangle = 6.9$.

these bursts can be regarded as being made up of a number of "pulses" having a typical separation of the order of 1 s (but which are *not* periodic). N96 found that the typical pulse shape is cuspy, similar to the peak near $t \simeq 1.5$ s in the top curve in Figure 6.

Comparing these findings to the results of §§ 3 and 4, we can identify three key points. First, the observed timescale of the order of 1 s between pulses is comparable to the predicted timescale (§§ 3.4 and 4), *but only if the lenses have low mass* ($\sim 10^{-8}\ M_\odot$) *or the sources are at high redshift.* Second, the typical "pulse" shape observed by N96 is similar to the $3 \rightarrow 1$, i.e., image-annihilating, caustic crossing discussed in § 3.2 and shown in Figures 4 and 6. However, the theory presented earlier in this paper gave no reason to suppose that $3 \rightarrow 1$ crossings should be preferred over $1 \rightarrow 3$ crossings, and in fact, one does expect both to be present. Both *are* present in the simulated light curves shown in Figures 7 and 8. One could appeal to an observational bias that favors $3 \rightarrow 1$ caustic crossings over their $1 \rightarrow 3$ counterparts because the high and cuspy peaks of the former render them more visible in the light curves (see, particularly, Fig. 4). However, this does not seem to us to be a strong argument. Finally, although the single fold-crossing events modelled in § 3 are obvious in the light curves, it is plain that *the simulations in § 4 do not yield sufficient modulation to be able to explain the profound variations seen in the data.*

On the last of the above points we note that there is no discrepancy between the calculations undertaken in § 3 and the simulations of § 4. The difference between the computed modulation depth in the two cases simply reflects the fact that the caustics present in the simulations exhibit more curvature in the lens mapping than was assumed in § 3.

5. PARALLAX

A key aspect of the lensing model we are investigating here is that of parallax. The importance of parallax phenomena depends on the spatial separation of the detectors that are employed, in comparison with the spatial scale on which the magnification pattern changes. In the low optical depth regime, the latter scale is given by

$$\left(4\frac{GM}{c^2}\frac{D_s D_d}{D_{ds}}\right)^{1/2} \simeq 60\sqrt{M_{-4}}\ \text{AU}\ , \qquad (22)$$

where D_s is the angular diameter distance of the source from the observer and to arrive at the numerical result we have assumed $z_s = 3$ and considered the median lens. Hence, for detectors separated by a few astronomical units, parallax might be expected to show up only for lenses of mass $M \lesssim 10^{-7}\ M_\odot$ (Nemiroff & Gould 1995). However, in the model we are considering the expanding source crosses caustics, and in the vicinity of caustics the magnification pattern varies significantly on spatial scales much smaller than given by equation (22). Indeed, at caustic crossings the transverse flux gradient is limited only by the source structure, and parallax may be observable even over very modest baselines. Specifically, if the width of the high-intensity ring of the source is taken to be 4×10^{-3} of the apparent radius (see § 4.2) and the latter is approximately 6 AU at $t = 10$ s ($E_{52} = n = \Gamma_3 = 1$), then parallax may be evident over transverse length scales as small as 4×10^{11} cm. In this circumstance the main instrumental requirement is for good temporal resolution in the detectors and high signal-to-noise ratio, so that the times at which caustic crossings occur can be precisely determined (Grieger, Kayser, & Refsdal 1986; Hardy & Walker 1996). GRBs are typically recorded with temporal resolution of tens of milliseconds, or better, often at high signal-to-noise ratios, so that the available timing precision is generally rather good. Moreover, we wish to emphasize that, provided that there are significant increases in flux associated with a caustic crossing, the ability to precisely time such an event is essentially independent of lens mass, and this parameter does not influence the detectability of the two parallax phenomena we describe.

5.1. *Displaced Burst Locations*

Suppose we observe a burst with a pair of identical detectors whose spatial separation is small in comparison with the scale on which the lens magnification pattern changes. The caustic network will appear very similar as seen from the two different locations, but with a slight shift on the sky in a direction parallel to the sky projection of the vector

separation between the detectors, $\boldsymbol{b}_{12} = \boldsymbol{x}_1 - \boldsymbol{x}_2$, and by an amount proportional to b_{12}. Consequently, the two light curves are almost identical in structure, but the caustic crossings are seen to occur at slightly different times at the two detectors. Thus, if burst time of arrival is used to determine which direction the wave front has arrived from, then the present model predicts that the inferred location of the source is shifted from the true location (see also the model of McBreen & Metcalfe 1988).

In the absence of any lensing phenomena, under the assumption of a source at infinity (plane wave front), a measured difference in arrival time, $\Delta t_{12} = t_2 - t_1$, between detectors tells us that the burst came from a direction defined by the unit vector $\hat{\boldsymbol{n}}$, such that $\hat{\boldsymbol{n}} \cdot \boldsymbol{b}_{12} = c\Delta t_{12}$. Thus, the source is constrained to lie on a circle of angular radius $\alpha := \cos^{-1}(c\Delta t_{12}/b_{12})$, centered on the direction $\hat{\boldsymbol{b}}_{12}$. If a timing offset δt_{12} is introduced, then the corresponding angular offset $\delta\alpha$ is given by $\sin\alpha\delta\alpha = -c(\delta t_{12}/b_{12})$. The timing difference that is expected as a result of parallax, in our model, is roughly $\delta t_{12} \lesssim \varpi \sin\alpha(b_{12}/\beta_{\rm ap}c)$ for any given caustic crossing. (The precise value of δt_{12} depends, of course, on the orientation of $\boldsymbol{b}_{12}$ relative to the orientation of the caustic.) Thus, for a burst that exhibits only a single caustic crossing event, the expected angular offset is

$$|\delta\alpha| \lesssim \frac{\langle\varpi\rangle}{\beta_{\rm ap}} \ . \tag{23}$$

Some caution should be exercised in applying this result because in our case, in which a network of caustics is present, the folds cannot be readily associated with individual lenses, and because the lenses are distributed along the whole line of sight, it is not clear how the effective value of ϖ should be estimated. We shall nevertheless employ equation (23) as if the values of ϖ were in one-to-one correspondence with lenses and use the median value of ϖ as given in equation (18). For a source at redshift $z_s = 3$, at an observed time $t \sim 10$ s after the start of the burst, equation (6) leads us to expect an apparent expansion speed of $\beta_{\rm ap} \simeq 320$, and projecting this into the observer's plane yields the result $|\delta\alpha| \lesssim 4'$. This estimate is valid for a burst that exhibits only a single caustic crossing; if the burst has temporal substructure with N_p peaks in the light curve, then we expect $|\delta\alpha|$ to be smaller by a factor of the order of $N_p^{1/2}$. We now turn to the question of whether such systematic errors are either evident in existing data or are significantly constrained by them.

Comparing burst arrival times between three spacecraft localizes any source to one of two possible intersections between three separate loci (one locus derived from each spacecraft pair). Because the observable quantity is the burst arrival time and each locus reflects the difference between a pair of arrival times, only two of these loci provide independent information on the burst location; in other words, the location is not determined with any redundancy if only three spacecraft are employed. If four or more interplanetary spacecraft are available for burst triangulation, then redundant positioning is possible, and systematic errors can therefore be revealed using only the triangulation data. Many bursts were redundantly positioned using the first generation of interplanetary GRB detectors (Atteia et al. 1987), and in two of these cases there were highly significant discrepancies (10 σ) between the localizations. However, in at least one of these two cases (GRB 790329) the cause of the discrepancy appears to be understood (Laros et al. 1985), and we adopt the conservative assumption that the other discrepant burst (GRB 790116) is also attributable to effects other than the parallax phenomenon under discussion here. The typical level of agreement between redundantly determined burst locations excludes errors at the level $|\delta\alpha| \gtrsim 1^\circ$ (Laros et al. 1985), but this result does not strongly constrain the model we have presented because offsets as large as this are expected only in exceptional circumstances. Specifically, offsets larger than 1° can only occur if the apparent expansion speed is $\beta_{\rm ap} < 60$ *and* the source is at low redshift ($z_s < 1$) *and* a caustic crossing event occurs.

There are no four-spacecraft triangulations available from the modern (BATSE and post-BATSE) era of GRB studies, and we have therefore searched the literature for bursts that have been accurately located by both triangulation and an independent method. The best sample of this type that we found is comprised of nine GRBs that were observed by BATSE, *Ulysses*, and either the *Pioneer Venus Orbiter* (Laros et al. 1998) or the *Mars Observer* (Laros et al. 1997)—for which triangulated positions are therefore available—all of which were independently positioned by the rotation modulation collimator of the WATCH experiment (Sazonov et al. 1998). The smallest error associated with the triangulated positions (1 σ statistical plus systematic) for these bursts is $20''$, while the median error is close to $3'$. Moreover, the WATCH error circles all have radii exceeding $14'$ (1 σ statistical plus systematic). Considering that we expect deviations of the order of an arcminute, the WATCH error circle, in particular, is so large that at first sight it seems hopeless to attempt to constrain the model via astrometry. The situation is not quite as bad as it first appears because pairs of Interplanetary Network (IPN) loci sometimes intersect at a very acute angle, in which case the location of the intersection point is very sensitive to any errors in α, thus allowing us to gauge the magnitude of the IPN errors. There are four examples of this type of configuration among our sample of bursts. However, none of the implied errors are highly significant when compared to the estimated measurement error, nor do these results provide any powerful constraints on the theoretical model. We have therefore relegated the details of our astrometric analysis of this sample to the Appendix, and in the present section we confine ourselves to a brief discussion of the outcome.

For the four bursts for which we could gauge the actual error in α, the mean error value is only 1.2 times the estimated error (1 σ statistical plus systematic) and is thus consistent with expectations. It is therefore appropriate to quote the results of our analysis in the form of upper limits. To do this, we take an upper limit of 3 σ in each of the four cases; in order to compare with our theoretical prediction (eq. [23]) we then convert to an upper limit on the typical parallax error on each caustic crossing by multiplying the 3 σ_α limit by $N_p^{1/2}$. The values of N_p for BATSE 451 and BATSE 1698 were taken from N96: $N_p = 4$ and 7, respectively. For BATSE 2387 and BATSE 907, examination of the archival light curves[5] reveals that $N_p = 1$ and $N_p \simeq 5$, respectively. The resulting limits on parallax for a single caustic crossing are thus deduced to be $|\delta\alpha| < 2\farcm7$, $37'$, $2\farcm6$, and $37'$ from BATSE 451, 907, 1698, and 2387, respectively. Even the lowest of these limits is only comparable to the

[5] See http://cossc.gsfc.nasa.gov.

predicted value ($\lesssim 4'$ for a caustic crossing occurring at $t = 10$ s and a source at redshift $z_s = 3$), and so we conclude that existing GRB astrometry does not significantly constrain the model we have presented.

5.2. *Burst Profiles*

For bursts lasting a few seconds or more, it is usually the case that the light curves contain several peaks. In a nanolensing model these would be identified with caustic crossings, with each peak marking the time at which the limb of the expanding source first touches the caustic. Now the relative timing offsets introduced by parallax are, of course, different for different caustics, so we expect that parallax should alter the time interval between the peaks of a given burst, as measured by physically separated (but otherwise identical) detectors. The effect is evident in Figure 9, which shows two simulations of an expanding source, as described in § 4.2, having slightly different initial burst locations. (In respect to the actual calculations undertaken, this is equivalent to displacing the observer and thus simulates the effect of parallax.) One of the caustic crossings visible in Figure 9 is seen at almost the same time ($t \simeq 0.013$) in both light curves, whereas the other is seen at different times in the two simulations. The expected timing difference is simply the quantity δt_{12}, estimated in § 5.1, and this evaluates to $|\delta t_{12}| \sim 1$ s for $z_s \simeq 3$, $b_{12} \sin\alpha \simeq 3$ AU, and $t \sim 10$ s. This value is much larger than the limiting time resolution of the *Ulysses* and BATSE instruments (Hurley et al. 1992; Fishman et al. 1994) and should therefore be detectable if the signal-to-noise ratio of the data is sufficiently high. Such measurements offer a very powerful test of the model we are proposing because both the anticipated size of the effect should render it measurable and *no other model mimics this behavior.* In particular, the test is more powerful than one based on apparent burst locations (§ 5.1) because there is no requirement for absolute timing information; only relative timing is important, and essentially all spacecraft yield relative timing information with high accuracy.

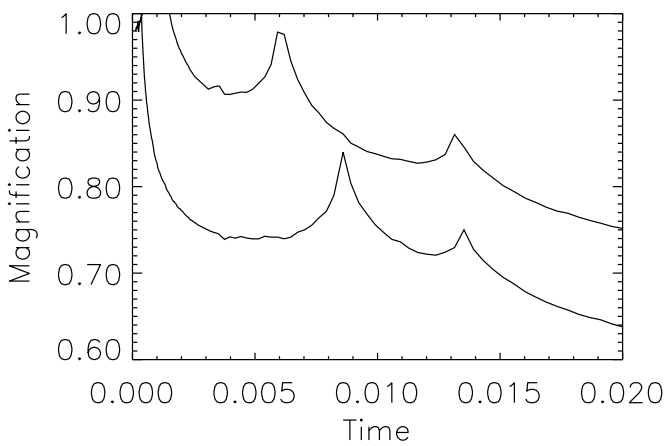

FIG. 9.—Effect of parallax on the nanolensing magnification curve of an expanding, self-similar ($m = 12$) blast wave ($\Delta = 4 \times 10^{-3}$). Time is shown here in units of the time taken for the source to expand to an apparent radius equal to the Einstein ring radius. The two curves differ in respect of the apparent source location, which is shifted by 1.4% of the Einstein ring radius (and the upper curve has been displaced by 0.1 in magnification for clarity). This is equivalent to shifting the observer's location by an amount 1 AU, transverse to the line of sight, if the lens mass is $10^{-4}\ M_\odot$ and the source redshift is $z_s = 5$.

To emphasize the clarity of this test, let us review what should be seen in the absence of any parallax effects. Two detectors observing in the same energy band should record source flux variations that, once the light curves have been shifted so as to align the times of burst onset, are in direct proportion to each other. Detector efficiency and spacecraft geometry ordinarily do not change significantly on timescales $\lesssim 100$ s, so a single constant of proportionality should hold throughout each burst. In the case of spacecraft in low Earth orbit, such as the *Compton Gamma-Ray Observatory*, some fraction of the sky is occulted by the Earth, and it is possible for ingress/egress to occur during a burst. But this is a rare phenomenon; moreover it is easily recognized and therefore not a concern in the present context. Particle backgrounds, and their trends with time, inevitably differ between any two detectors, but in normal circumstances they also change relatively little on the timescale of a GRB, and a linear trend in the background over the duration of the burst is a suitable model for most purposes. Electron precipitation events constitute a variable particle background in low Earth orbit that in some respects can mimic a GRB (Horack et al. 1992); however, these events are readily distinguished from GRBs by comparing count rates among the BATSE detectors. Finally, detector dead time introduces nonlinearity (different for different detectors) that can significantly affect the recorded light curve, causing the count rate to saturate if the burst is bright. Saturation will not affect the peak location because the recorded count rate is a monotonic function of the flux, but will displace the burst centroid; however, saturation can be recognized trivially, from the count rate, and affected bursts can be excluded from consideration. In summary, none of the effects described above should be confused with the parallax signal we have discussed.

In practice, testing for parallax effects will *not* be done with a pair of matched detectors, but with whatever instrumentation is available in the IPN, so we will be comparing data from detectors with different energy responses. This presents us with a potential problem in that many of the pulses that are seen in GRB light curves exhibit spectral evolution (N96) and therefore have different shapes in different energy bands. Consequently, with imperfect knowledge of the (evolving) burst spectrum or the energy response of either of the detectors, the pulse will appear to be slightly shifted in time, and this effect can mimic a parallactic timing offset. Fortunately, not all pulses are of this type (N96); a good fraction of pulses are narrow, time-symmetric events, whose peak and centroid locations are insensitive to photon energy (N96). This subset of pulses allows parallax searches to be attempted even with detectors that are not closely matched in their energy response.

A large number of GRB light curves are freely available at the BATSE archive[6] with 64 ms resolution in each of four energy bands. For comparison with these data, we have searched the literature for published GRB light curves from the *Ulysses* spacecraft (Hurley et al. 1992). This comparison offers very large baselines (up to 6.3 AU), for which the timing offsets should be correspondingly large. Although *Ulysses* has detected a large number of GRBs, including hundreds that were also detected by BATSE (Hurley et al. 1999a, 1999b), we were able to find only three published

[6] See http://cossc.gsfc.nasa.gov/batse.

Ulysses light curves for GRBs in the BATSE catalog. Two of these—BATSE 2151 (GRB 930131, the "Super Bowl Burst"; Hurley et al. 1994) and BATSE 143 (GRB 910503; Hurley 1992)—have very modest projected separations between the spacecraft (1.4 and 1.6 AU, respectively). We have therefore focussed our attention on BATSE 1663 (GRB 920622), for which the *Ulysses*-BATSE projected separation (i.e., transverse to the line of sight to the burst) was 3.8 AU. This burst has been analyzed in detail by Greiner et al. (1995).

We digitized the *Ulysses* light curve directly from Figure 1 of Greiner et al. (1995), and this light curve is reproduced in Figure 10, together with the BATSE light curve for the same interval. The BATSE data we plot here are the sum of the two lowest energy channels only, corresponding to the photon energy range 25–100 keV; this range is similar to the sensitive range of the *Ulysses* detector (15–150 keV; Hurley et al. 1992). The BATSE data have had a linear background subtracted from them; the background model was determined by taking the median values of 1 minute intervals starting 3 minutes before and 4 minutes after burst onset. (This procedure could not be used for the *Ulysses* data because the published light curve does not span a large enough time interval.) The two light curves were then aligned in time such that their cross-correlation is maximized, and an estimate of the *Ulysses* detector background was made by maximizing the cross-correlation as a function of assumed background, at constant temporal offset. (We note that varying the assumed background yielded insignificant changes in the temporal alignment.) The estimated *Ulysses* background was in this way found to be 107 counts bin^{-1}; the peak value of the normalized cross-correlation between light curves is 0.974.

Although the temporal alignment between the two spacecraft was determined to a precision of 10 ms, the accuracy of the procedure is poorer than this. We estimated the uncertainties associated with our method by cross-correlating the *Ulysses* data with the two highest energy BATSE channels. These data are for the same burst, but represent photons of energies higher than those to which *Ulysses* is sensitive. This procedure yielded an alignment that differed by 70 ms and a background rate that differed by 2 counts bin^{-1}, when referred to the results of the cross-correlation with the lowest energy BATSE data. Our method can be reasonably expected to be in error by less than the shifts exhibited here.

The flux scale in Figure 10 is chosen to be that of the *Ulysses* data, and the BATSE count rates have been rescaled accordingly (and we have then added a constant background of 107 counts bin^{-1} to the scaled BATSE data). This choice is appropriate because the BATSE data are of much higher signal-to-noise ratio than the *Ulysses* data, and the *Ulysses* flux scale is thus germane to the statistical significance of any comparison between the two. We have also rebinned the BATSE data from the original value of 64 to the 250 ms of the *Ulysses* data, and for clarity we have offset the BATSE data by -100 counts bin^{-1}. It can be seen from Figure 10 that the BATSE and *Ulysses* light curves are very similar, as expected, although there are some evident differences in the $t = 16$–19 s region, and the *Ulysses* light curve seems to manifest more fluctuations in the region $t > 20$ s than would be expected on the basis of the BATSE light curve. Quantitatively, we can say that the BATSE data form an acceptable model of the *Ulysses* data, with a χ^2 statistic of 76 for the difference between the two, over the first 19 s of the burst, with $(19/0.25) - 3 = 73$ degrees of freedom.

However, the key question for us here is not the overall similarity of the two light curves but whether or not the temporal substructure occurs at different times at the two spacecraft. In Figure 11 we concentrate our attention on the central region of the burst, where the BATSE light curve manifests obvious substructure. In particular, the regions $t = 7.5$–12 and 14.5–19 s show a number of peaks that one can use to test the model. We can compute the combined χ^2 of these intervals: it is $\chi^2 = 48.5$, with 36 degrees of freedom. Clearly, the BATSE-derived model does not perform as well in these intervals with temporal substructure as it

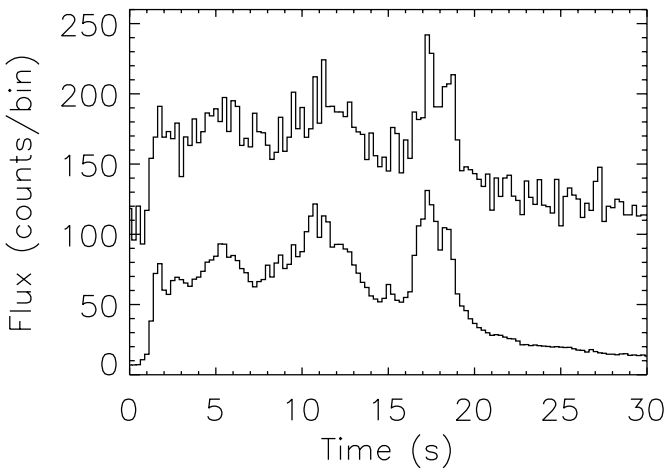

FIG. 10.—*Ulysses* data for GRB 920622 (BATSE 1663; Greiner et al. 1995), together with the light curve derived from the sum of count rates from BATSE channels 1 and 2. The BATSE data have been background subtracted, then aligned and scaled appropriately by cross-correlating with the *Ulysses* data, as described in § 5.2. The BATSE data have been rebinned to match the binning of the *Ulysses* data and have been offset by -100 counts bin^{-1} for clarity of presentation. The signal-to-noise ratio of the BATSE data is very high, and all of the features visible in the BATSE light curve are real. The flux scale is appropriate to the *Ulysses* data.

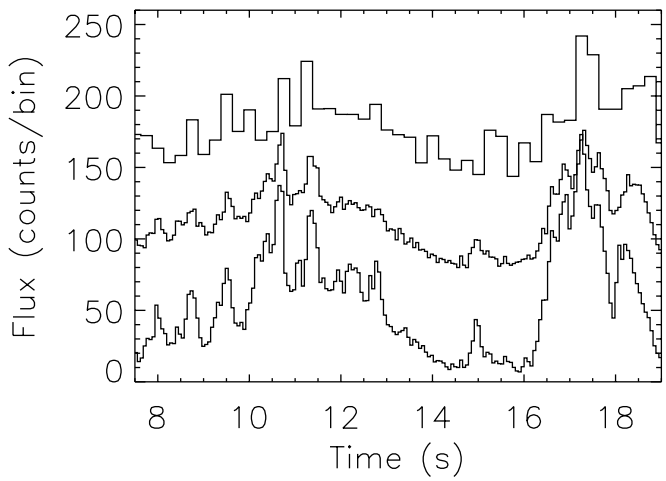

FIG. 11.—Portion of the two light curves shown in Fig. 10. Here the BATSE high-energy channels are shown (*bottom curve*) in addition to the low-energy data (*middle curve*) and the *Ulysses* data (*top curve*); both BATSE light curves are shown at their original resolution (64 ms). The low-energy and high-energy light curves have been offset by -70 and -130 counts bin^{-1}, relative to their modelled location, for clarity of presentation.

does elsewhere; however, the model is still acceptable, with this value of χ^2 being realized by chance in 8% of trials. Moreover, a simple χ^2 test does not reveal whether the model is performing poorly because the temporal substructure is shifted in time or for some other reason such as the different energy response of the *Ulysses* detector compared to the combination of BATSE channels 1 and 2.

Examination of Figure 11 suggests that both of these effects may play a role. In particular, we note that the feature in the low-energy BATSE light curve just after $t = 18$ s is clearly chromatic, with a centroid that occurs earlier at higher energies, and we must therefore allow that in the *Ulysses* data this feature may exhibit a profile different from the BATSE model. By contrast, at $t = 15$ s, the BATSE model shows a well-defined event, for which we can tentatively identify a counterpart peak in the *Ulysses* light curve, but this counterpart occurs 0.4 s later. Although there is some difference in the profiles of this event between high- and low-energy BATSE light curves, it does not seem reasonable to attribute the BATSE-*Ulysses* shift to chromatic effects because the differences are modest, whereas the shift is comparable to the width of the feature. Another case in which the data suggest a temporal offset occurs around $t = 11$ s. Here we find two narrow, approximately time-symmetric peaks in the BATSE model. In the *Ulysses* data there is no question about which peaks to identify as their counterparts—the two unresolved peaks either side of $t = 11$ s—but the second peak appears earlier in the *Ulysses* data than in the BATSE model. It does not seem reasonable to attribute this to chromatic effects because the profiles of the low- and high-energy BATSE data are quite similar. However, we still cannot be confident of having found an example of the effect we are looking for because (1) the peak is so narrow that it is undersampled in the *Ulysses* light curve and (2) the modest signal-to-noise ratio of these peaks in the *Ulysses* data means that any comparison cannot yield highly statistically significant results.

In summary, we have compared published *Ulysses* data with archival BATSE data for a single burst having a large projected separation between spacecraft. This comparison yielded some hints of parallax, but the evidence is of low statistical significance and therefore not compelling. By reprocessing the raw *Ulysses* data—which have a temporal resolution 8 times finer than the published light curve—it should be possible to make a more meaningful comparison between the two data sets. In particular, the higher temporal resolution would be valuable in studying the peaks close to $t = 11$ s, which are unresolved in the published *Ulysses* light curve. A further improvement on our analysis would be to derive a model light curve using the point-by-point spectral data ("colors") derived from BATSE, together with the spectral response matrices of the two spacecraft.

6. DISCUSSION

Although the burst (BATSE 1663) studied in § 5.2 was chosen for its relatively large projected separation between the spacecraft, it is not extreme in this respect, and there are ~80 instances (Hurley et al. 1999a, 1999b) of larger projected separations among the bursts detected by both BATSE and *Ulysses*. Indeed, the principal criterion for using the BATSE 1663 data was that the data are published. This burst merited detailed study, and hence publication of the light curve, because it happened to occur within the COMPTEL field of view (Greiner et al. 1995). Among the many other bursts in which one might consider searching for parallax, how is one to choose? The expected temporal offset is large (see § 5.1) if (1) the projected baseline $b_{12} \sin \alpha$ between spacecraft is large, (2) the source redshift is low (hence $\varpi \simeq 1$), and (3) the apparent expansion speed of the source ($\beta_{\rm ap}$) is low. Unfortunately only the first of these criteria can be securely determined directly from the data at hand. However, if all other parameters are held fixed, then we expect that high expansion speed and high source redshift would both lead to large numbers of caustic crossing events, so it makes sense to select bursts that exhibit a small number of peaks in their light curves. Ideally, the overlap among these peaks should be small, so that the properties of each peak can be characterized more-or-less independently of the others. These criteria also help to avoid the potential problem of peak confusion: if parallax displaces a burst peak by an amount comparable to the separation between peaks in one of the light curves, then it becomes difficult to identify counterparts between the light curves from the different spacecraft. Finally, and most obviously, a significant detection absolutely requires high signal-to-noise ratio, so bright bursts are strongly preferred.

If we could increase the baseline between the two detectors beyond the few astronomical units that characterize interplanetary spacecraft, our model predicts that the amplitude and location of the substructure peaks would differ more and more as the baseline increased, and it would eventually become difficult to identify counterpart peaks between the two profiles. Ultimately, if the separation were to reach values $\gtrsim 60 M_{-4}^{1/2}$ AU, the entire caustic pattern would differ as seen from the two locations, and there would consequently be little resemblance between the recorded burst profiles. Although there seems to be no immediate prospect of separating a pair of detectors by such a large distance, it is nevertheless possible to reach this regime, and thus to observe completely different profiles, if a GRB is "macroscopically" gravitationally lensed. More specifically, if a gravitational lens forms multiple images that are split by an angle very much greater than $15 M_{-4}^{1/2}$ nas, then the caustic crossings seen in each image will bear little resemblance to one another. This, of course, would be true even for micro- (arcsecond) lensing due to stars at cosmological distances. Thus, in the case of lensing by galaxies, and aggregates of larger mass, any lensed "echo" should exhibit a different temporal profile to that of the counterpart signal that arrives first (see also Williams & Wijers 1997; Paczyński 1986b; Blaes & Webster 1992). It is expected that gravitational lensing by galaxies should yield echoes of roughly 0.1% of bursts (Paczyński 1986b; Mao 1992), but this effect has never been clearly detected. The null results to date (Nemiroff et al. 1994; Marani et al. 1999) are not highly statistically significant, nor is it trivial to recognize echoes even if they are simply scaled copies of the "original"—see Wambsganss (1993) and Nowak & Grossman (1994). This means that the lack of any identified echoes, while consistent with the present model, is not a decisive argument in its favor. On the other hand, if examples were found with complex temporal substructure faithfully reproduced in an echo, then it follows that the observed substructure is not due to gravitational nanolensing.

It has previously been noted that if the universe is populated with low-mass lenses, then interference phenomena may manifest themselves in GRB data (Gould 1992; Stanek,

Paczyński, & Goodman 1993; see also Deguchi & Watson 1986). The lens masses for which this effect is relevant are usually thought to be many orders of magnitude smaller than the planetary-mass bodies considered here. In the case of lensing by a fold, where the angular splitting of the images vanishes for a source located precisely on the caustic, interference fringes can be realized for larger masses than in the case of isolated gravitational lenses. However, strong interference fringes also require that the source be at most comparable in size to the Fresnel scale—$(D_s\lambda)^{1/2}$ for wavelength λ—otherwise the fringe patterns from different regions of the source manifest their maxima at quite different locations, and the fringe visibility (contrast) is much reduced. We have already estimated (§ 5) the thickness of the high-intensity limb of the source to be $\sim 4 \times 10^{11}$ cm, so with $D_s \sim 4$ Gpc we can expect interference phenomena to be important only for $\lambda \gtrsim 10^{-5}$ cm, i.e., longward of the far-ultraviolet region, for the source model we have employed.

It is worth noting that the presence of a caustic network on nanoarcsecond scales has no immediate implications for the observable properties of the GRB afterglow because at this late stage in its evolution the observable emission from the blast wave extends over angular scales that are so large that the net magnification is very close to the mean magnification. Microlensing of the afterglow is, however, possible (Loeb & Perna 1998; Mao & Loeb 2001) because the characteristic angular scale of the magnification pattern is much larger in this case.

The two main discrepancies, which we noted in § 4, between the modelled nanolensing variations and the observed temporal structure in GRB light curves are the small amplitude and long timescale of the nanolensing fluctuations. Given that the model parameters appropriate to real sources are typically not known with any accuracy, one could try to evade the second of these discrepancies by considering sources at high redshift. Specifically, as the source redshift approaches $z_s = 10.6$, corresponding to nanolensing optical depth $\tau = 1$, the caustic density becomes very large indeed, and the variability timescale correspondingly decreases (§ 3.4). Thus, the observed characteristic timescale of the order of 1 s between "pulses" (N96) matches the nanolensing variability timescale only for very low mass lenses ($\sim 10^{-8}\ M_\odot$) at $z_s = 1$, but for sources at $z_s \sim 10$, the implied lens mass would correspond to that ($\sim 10^{-4}\ M_\odot$) deduced from the data on quasars (Schneider 1993; Minty 2001). This idea is, however, quickly disposed of because as the angular scale of the caustic network shrinks, so does the width of the high-magnification regions close to the caustics. In turn this means that a source of given size will exhibit smaller variations as it crosses the caustics, exacerbating the other notable discrepancy between the nanolensing simulations and the observed variability. This aspect of gravitational lensing at high optical depth, where the depth of modulation vanishes for nonpointlike sources as $\tau \to 1$, is well known (Deguchi & Watson 1987).

We wish to draw attention to the fact that all of the results reported in the present paper are for shear-free environments, and if a large external beam shear is present, then the properties of any nanolensing can be quite different. High shear is expected if, for example, nanolensing occurs close to a microlensing caustic. Calculations appropriate to this circumstance will be reported elsewhere (M. A. Walker & G. F. Lewis 2003, in preparation).

7. CONCLUSIONS

Motivated by an existing interpretation of quasar variability in terms of gravitational nanolensing, we have examined the implications of this model for the observed properties of GRBs. Using a self-similar blast wave model to represent the source (no intrinsic variability), we find that the light curves of some of the caustic crossings resemble those of the "pulses" commonly seen in GRBs, and for high-redshift sources, the timescale of the predicted nanolensing variations is consistent with the GRB data. However, the predicted depth of nanolensing modulation is far too small to explain the deep variations observed in GRBs, and this problem is exacerbated if the GRBs are at high redshift. These results mean that the GRB data do not exclude the nanolensing interpretation of quasar variability; conversely, the simplest (shear free) nanolensing model cannot explain the observed GRB variability. Despite this failure, there are weak indications in the published IPN data that nanolensing may actually be responsible for some of the observed variations of GRBs: the light curves for one GRB show hints of parallax. This effect is uniquely associated with lens-induced variations and thus motivates a careful examination of existing IPN data.

M. A. W. much appreciates the hospitality of the Raman Research Institute, where this work was begun. We have benefitted greatly from many helpful discussions with Dipankar Bhattacharya, Sunita Nair, and P. Sreekumar, all of whom came within a hair's breadth of being coauthors on the present paper. G. F. L. would like to thank Joachim Wambsganss for providing his ray-tracing code and David Bowie for his Low album. We thank the referee, Robert Nemiroff, for helpful comments.

APPENDIX

GAMMA-RAY BURST ASTROMETRY

In this Appendix we give details of the astrometric analysis of the sample of bursts referred to in § 5.1. The sample was drawn from the nine bursts observed by BATSE, *Ulysses*, and the *Mars Observer* spacecraft (Laros et al. 1997), plus the 37 bursts observed by BATSE, *Ulysses*, and the *Pioneer Venus Orbiter* (Laros et al. 1998). BATSE was capable of localizing sources in its own right, by comparing the count rates recorded in different detectors, each pointing in a different direction. This was not, however, a simple facility to implement in practice (Pendleton et al. 1999), and the resulting localizations are only accurate to a few degrees—this point has been directly verified by comparing the positions of solar flares, as located by BATSE, with the position of the Sun (Brock et al. 1992). Consequently, although BATSE localizations are useful in lifting the degeneracy between the two intersection points of the IPN loci, they are not accurate enough to reveal systematic errors in the

TABLE 1
ASTROMETRY OF GAMMA-RAY BURST SOURCES

	IPN Loci				WATCH						
BATSE Trigger (1)	R.A. (J2000.0) (deg) (2)	Decl. (J2000.0) (deg) (3)	α (deg) (4)	$3\sigma_\alpha$ (deg) (5)	R.A. (J2000.0) (deg) (6)	Decl. (J2000.0) (deg) (7)	σ_w (deg) (8)	Π_0 (9)	$\Pi_{\min}$ (10)	$\delta\alpha_{\min}$ (σ_α) (11)	$\lvert\delta\alpha_{\min}\rvert$ (arcmin) (12)
451*	134.8255	18.4232	66.8162	0.0119	...	...	...	...	...	...	...
	133.5243	18.7903	68.0884	0.0226	199.60	−02.60	0.41	44	1.56	1.07	0.48
907*	342.4405	−08.6911	44.1528	0.0641	...	...	...	...	...	...	...
	342.9264	−08.8461	44.5370	0.2785	297.37	−04.71	0.56	944	3.03	1.09	6.0
1141	168.0347	06.4847	30.0358	0.0472	...	...	...	...	...	...	...
	160.4516	09.2822	34.6366	0.2360	171.97	−22.59	0.57	2.74	2.39	−0.50	2.3
1473	155.1400	10.0896	51.2649	0.0096	...	...	...	...	...	...	...
	157.1525	08.8837	51.0046	0.0100	132.25	−36.39	0.22	0.09	0.08	−0.07	0.01
1538	332.4865	−09.1834	32.9477	0.0137	...	...	...	...	...	...	...
	338.9289	−07.6437	33.7998	0.0189	323.07	22.53	0.29	1.01	1.00	0.10	0.04
1698*	152.2635	05.1023	74.4660	0.0099	...	...	...	...	...	...	...
	161.6670	−00.9283	63.3050	0.0164	221.43	−30.75	0.26	7.14	4.19	0.32	0.11
1712	152.9064	04.6545	17.1004	0.2556	...	...	...	...	...	...	...
	130.6922	19.5520	33.6130	0.3669	145.67	−11.20	0.41	1.45	1.34	0.31	2.3
2387*	143.9743	−11.1837	63.9320	0.0520	...	...	...	...	...	...	...
	141.8929	−23.8803	51.5670	0.6170	109.24	−71.20	0.30	1195	5.75	−2.24	28
2431	326.3289	11.8938	54.6810	0.0060	...	...	...	...	...	...	...
	317.3416	23.2362	55.8180	0.0120	281.42	−20.18	0.24	0.58	0.58	0.04	0.01

NOTE.—Cols. (2) and (3) give the right ascension and declination of the center of the IPN loci, with the corresponding dimensions of the annulus being prescribed by the angular radius, α (col. [4]) and its associated error, σ_α (col. [5]). Columns (6) and (7) give the right ascension and declination for the WATCH localization, with the radius of the error circle, σ_w, in col. (8). Cols. (9)–(12) give properties of the penalty function, Π (eq. [A1]), as deduced for each burst. Asterisks indicate that the actual error in α can be gauged for this burst because $\Pi_0 - \Pi_{\min} \gg 1$.

triangulation procedure at the arcminute level we are interested in.[7] To constrain any such errors, we therefore employed the localizations that were obtained by the WATCH experiment, quite independently of the triangulated positions. This experiment employed a rotation modulation collimator to locate sources, typically with accuracies better than half a degree (at the 1 σ level; Sazonov et al. 1998). The additional requirement that each burst have been observed by WATCH necessarily decreases the sample size, and we are left with only nine bursts in our final sample; these bursts and the corresponding astrometric information are listed in Table 1, while the localizations themselves are presented graphically in Figure 12.

It is immediately apparent from Table 1 that the WATCH error circles are too large to determine positional errors at the level of a few arcminutes (which is the upper end of the range expected for $\delta\alpha$ in the blast wave model—see § 5.1). However, as can be seen from Figure 12, there are a number of instances in this sample in which the loci derived from burst timing intersect at a very acute angle, and in these cases the intersection point of the loci is displaced on the sky by an amount $\gg \delta\alpha$, so that errors of the anticipated size might possibly be revealed by comparison with the WATCH localizations. To test this possibility, we have employed a penalty, $\Pi(\delta\alpha)$, which is a function of the offset $\delta\alpha$ in the radius α of one of the loci:

$$\Pi(\delta\alpha) = \left(\frac{\delta\alpha}{\sigma_\alpha}\right)^2 + \left(\frac{\xi}{\sigma_w}\right)^2, \tag{A1}$$

where $\xi = \xi(\delta\alpha)$ is the angular separation between the intersection of the IPN loci and the WATCH location, σ_w is the estimated error in the WATCH location (one-third of the 3 σ statistical error, plus the systematic error, as quoted by Sazonov et al. 1998), and σ_α is the estimated error in the determination of α (one-third of the 3 σ statistical-plus-systematic error quoted by Laros et al. 1997, 1998). The location ($\delta\alpha_{\min}$) of the minimum value $\Pi_{\min}$ of this penalty function can, in some cases, give us an estimate of the value of $\delta\alpha$. One point to note is that the WATCH error distribution is ellipsoidal, but we are approximating it by a circular distribution.

Generally speaking, of the three loci derived from burst timing, one (corresponding to the BATSE-*Ulysses* baseline) has by far the smallest errors, and our adopted procedure is therefore to treat this locus as an absolute constraint on the burst location. We then discard the annulus with the largest estimated error and use the remaining locus to determine the

[7] At this point we should draw attention to the anomalous case of BATSE 2475, reported by Laros et al. (1997), which apparently displayed an IPN intersection that was significantly discrepant even with respect to the rather crude BATSE localization. Having no way of understanding this result, Laros et al. (1997) were obliged to conclude that the *Mars Observer* had not detected the GRB detected by the other spacecraft and had in addition responded to another (unspecified) event, which in turn was not detected by the other spacecraft in the network, despite having the characteristics of a GRB. This coincidence seems rather contrived. An alternative explanation for the timing/position anomaly of this burst can be found in terms of parallax (§ 5 of the present paper), provided that BATSE 2475 exhibited a low expansion speed, with $\beta_{\rm ap} \lesssim 40$. (This conclusion assumes a low-redshift burst, which nevertheless manifests a caustic crossing event, and makes use of the BATSE localization given by Meegan et al. 1996.) However, we note that the reported discrepancy between BATSE and *Mars Observer* count rates for BATSE 2475 cannot be so readily explained.

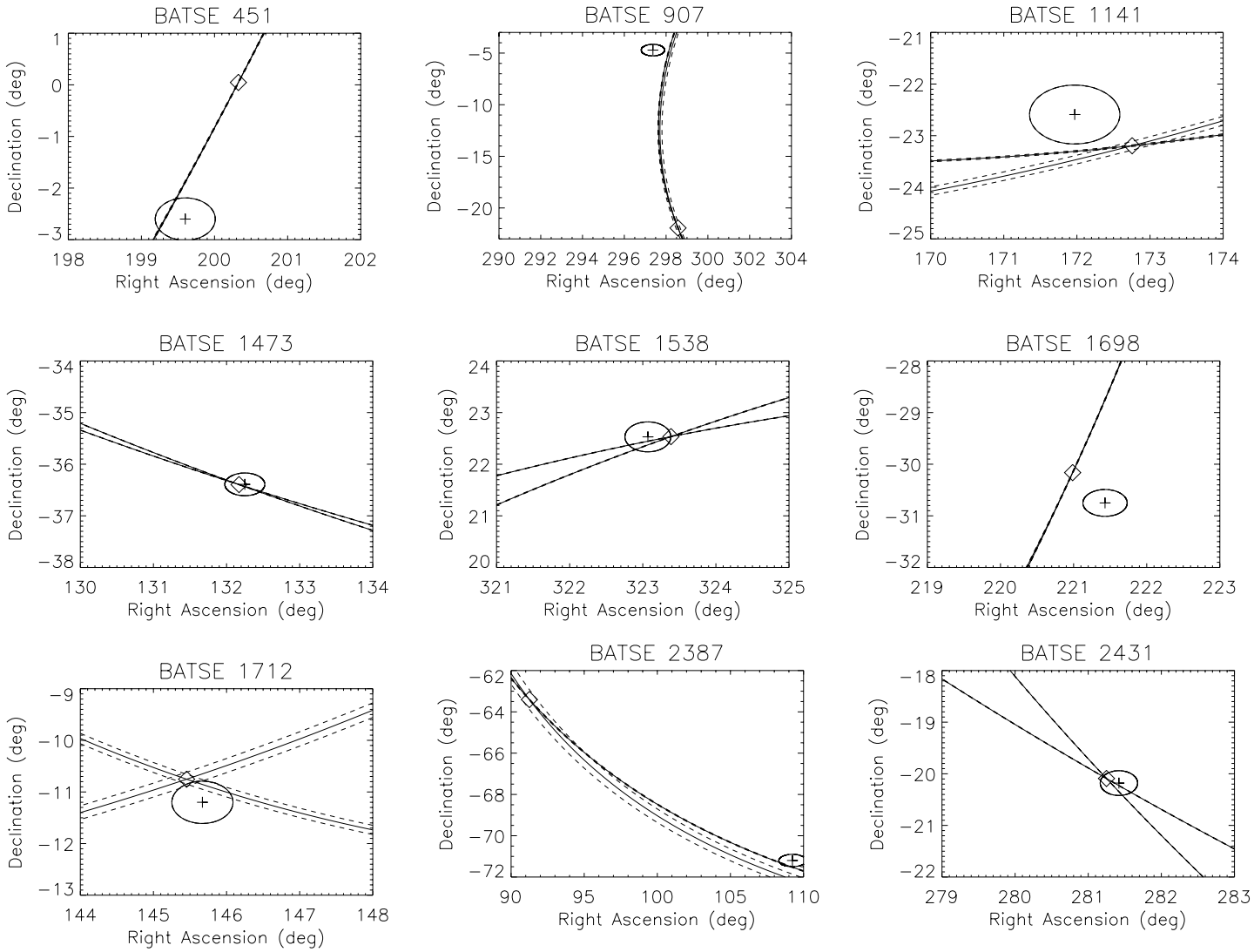

FIG. 12.—Positions for a sample of nine bursts that were located by both the WATCH instrument—crosses, with 1 σ (statistical plus systematic) error circles—and the IPN (*Ulysses* plus BATSE and either PVO or MO). IPN loci are shown (*solid line*), with ± 1 σ errors (statistical plus systematic: *dashed line*). A diamond marks the intersection of the IPN loci in each case.

intersection point. The radius of this second locus is then allowed to vary by an amount $\delta\alpha$, over a range $\pm 5\ \sigma_\alpha$, and for each value of $\delta\alpha$ we compute the separation ξ and thus the value of the penalty $\Pi(\delta\alpha)$. In general, the value of $\Pi_0 \equiv \Pi(0)$ will not coincide with the minimum value of the function, $\Pi_{\min} = \Pi(\delta\alpha_{\min})$, and if $\Pi_0 - \Pi_{\min} \gg 1$, then it is clear from the definition of Π that this means $\delta\alpha_{\min}$ is distinguishable from zero. The ratio $\delta\alpha_{\min}/\sigma_\alpha$ tells us whether the actual error that we have detected is significantly larger than the expected error in α. The results of this procedure are given in Table 1, where it can be seen that there are four bursts (BATSE 451, 907, 1698, and 2387) for which Π_0 is significantly greater than $\Pi_{\min}$. With the possible exception of BATSE 2387, the errors that we measure in these cases (i.e., $\delta\alpha_{\min}$) are only as large as one would expect, given the estimated error σ_α in each case. Of course, it remains possible that the systematic error we are looking for is in fact a major contribution to the estimated value of σ_α, and we are unable to exclude this possibility with the information at hand.

REFERENCES

Alcock, C., et al. 1998, ApJ, 499, L9
Ashman, K. M. 1992, PASP, 104, 1109
Atteia, J. L., et al. 1987, ApJS, 64, 305
Baring, M. G., & Harding, A. K. 1997, ApJ, 491, 663
Blaes, O. M., & Webster, R. L. 1992, ApJ, 391, L63
Blandford, R.D., & McKee, C.F. 1976, Phys. Fluids, 19, 1130
Blumenthal, G., Faber, S. M., Primack, J. R., & Rees, M. J. 1984, Nature, 311, 517
Brock, M. N., Meegan, C. A., Roberts, F. E., Fishman, G. J., Wilson, R. B. Paciesas, W. S., & Pendleton, G. N. 1992, in AIP Conf. Proc 265, Gamma-Ray Bursts, ed. W. S. Paciesas & G. J. Fishman (New York: AIP), 383
Bromm, V., & Loeb, A. 2002, ApJ, 575, 111
Canizares, C. R. 1982, ApJ, 263, 508
Carr, B. 1994, ARA&A, 32, 531
Cavallo, G., & Rees, M. J. 1978, MNRAS, 183, 359
Cohen, E., Piran, T., & Sari, R. 1998, ApJ, 509, 717
Costa, E., et al. 1997, Nature, 387, 783
Dalcanton, J. J., Canizares, C. R., Granados, A., Steidel, C. C., & Stocke, J. T. 1994, ApJ, 424, 550
Davis, M., Efstathiou, G., Frenk, C. S., & White, S. D. M. 1985, ApJ, 292, 371
Deguchi, S., & Watson, W. D. 1986, ApJ, 307, 30
———. 1987, Phys. Rev. Lett., 59, 2814
Dermer, C. D., & Mitman, K. E. 1999, ApJ, 513, L5
Djorgovski, S. G., et al. 1997, Nature, 387, 876

Draine, B. T. 1998, ApJ, 509, L41
Fenimore, E. E., Epstein, R. I., & Ho, C. 1993, A&AS, 97, 59
Fenimore, E. E., Madras, C. D., & Nayashkin, S. 1996, ApJ, 473, 998
Fenimore, E. E., Ramirez-Ruiz, E., & Wu, B. 1999, ApJ, 518, L73
Fishman, G. J., et al. 1994, ApJS, 92, 229
Frail, D. A., Kulkarni, S. R., Nicastro, L., Feroci, M., & Taylor, G. B. 1997, Nature, 389, 261
Gaudi, B. S., Granot, J., & Loeb, A. 2001, ApJ, 561, 178
Gould, A. 1992, ApJ, 386, L5
Granot, J., & Loeb, A. 2001, ApJ, 551, L63
Granot, J., Piran, T., & Sari, R. 1999, ApJ, 513, 679
Greiner, J., et al. 1995, A&A, 302, 121
Grieger, B., Kayser, R., & Refsdal, S. 1986, Nature, 324, 126
Hardy, S. J., & Walker, M. A. 1995, MNRAS, 276, L79
Hawkins, M. R. S. 1993, Nature, 366, 242
———. 1996, MNRAS, 278, 787
Horack, J. M., Fishman, G. J., Meegan, C. A., Wilson, R. B., & Paciesas, W. S. 1992, in AIP Conf. Proc 265, Gamma-Ray Bursts, ed. W. S. Paciesas & G. J. Fishman (New York: AIP), 373
Hurley, K. 1992, in AIP Conf. Proc 265, Gamma-Ray Bursts, ed. W. S. Paciesas & G. J. Fishman (New York: AIP), 3
Hurley, K., Briggs, M. S., Kippen, R. M., Kouveliotou, C., Meegan, C., Fishman, G., Cline, T., & Boer, M. 1999a, ApJS, 120, 399
———. 1999b, ApJS, 122, 497
Hurley, K., Sommer, M., Fishman, G., Kouveliotou, C., Meegan, C., Cline, T., Boër M., & Niel, M. 1994, in AIP Conf. Proc. 307, Gamma-Ray Bursts, ed. G. Fishman (New York: AIP), 369
Hurley, K., et al. 1992, A&AS, 92, 401
Kobayashi, S., Piran, T., & Sari, R. 1997, ApJ, 490, 92
Laros, J. G., et al. 1985, ApJ, 290, 728
———. 1997, ApJS, 110, 157
———. 1998, ApJS, 118, 391
Lewis, G. F., & Ibata, R. A. 2001, ApJ, 549, 46
Loeb, A., & Perna, R. 1998, ApJ, 495, 597
Mao S. 1992, ApJ, 389, L41
Mao S., & Loeb, A. 2001, ApJ, 547, L97
Marani, G. F., Nemiroff, R. J., Norris, J. P., Hurley, K., & Bonnell, J. T. 1999, ApJ, 512, L13
McBreen, B., & Metcalfe, L. 1988, Nature, 332, 234
Meegan, C. A., et al. 1996, ApJS, 106, 65
Mészáros, P., & Rees, M. J. 1997, ApJ, 476, 232
Metcalf, R. B., & Silk, J. 1999, ApJ, 519, L1
Metzger, M. R., Djorgovski, S. G., Kulkarni, S. R., Steidel, C. C., Adelberger, K. L., Frail, D. A., Costa, E., & Frontera, F. 1997, Nature, 387, 878
Minty, E. M. 2001, Ph.D. thesis, Univ. Edinburgh
Minty, E. M., Heavens, A. F., & Hawkins, M. R. S. 2002, MNRAS, 330, 378
Nemiroff, R. J., & Gould, A. 1995, ApJ, 452, L111
Nemiroff, R. J., Wickramasinghe, W. A. D. T., Norris, J. P., Kouveliotou, C., Fishman, G. J., Meegan, C. A., Paciesas, W. S., & Horack, J. 1994, ApJ, 432, 478
Norris, J. P., Nemiroff, R. J., Bonnell, J. T., Scargle, J. D., Kouveliotou, C., Paciesas, W. S., & Fishman, G. J. 1996, ApJ, 459, 393 (N96)
Nowak, M. A., & Grossman, S. A. 1994, ApJ, 435, 557
Paczyński, B. 1986a, ApJ, 301, 503
———. 1986b, ApJ, 308, L43
———. 1995, PASP, 107, 1167
Paczyński, B. 2001, in Supernovae and Gamma-Ray Bursts: The Greatest Explosions since the Big Bang, ed. M. Livio, N. Panagia, & K. Sahu (Cambridge: Cambridge Univ. Press), 1
Paczyński, B., & Rhoads, J. E. 1993, ApJ, 418, L5
Peebles, P. J. E. 1993, Principles of Physical Cosmology (Princeton: Princeton Univ. Press)
Pendleton, G., et al. 1999, ApJ, 512, 362
Press, W. H., & Gunn, J. E. 1973, ApJ, 185, 397
Rafikov, R. R., & Draine, B. T. 2001, ApJ, 547, 207
Rauch, K. P. 1991, ApJ, 374, 83 (erratum 383, 466)
Rees, M. J., & Meszáros, P. 1992, MNRAS, 258, P41
———. 1994, ApJ, 430, L93
Sari, R., & Piran, T. 1997, ApJ, 485, 270
Sazonov, S. Y., Sunyaev, R. A., Terekhov, O. V., Lund, N., Brandt, S., & Castro-Tirado, A. J. 1998, A&AS, 129, 1
Schild, R. E. 1996, ApJ, 464, 125
Schneider, P. 1993, A&A, 279, 1
Schneider, P., Ehlers, J., & Falco, E. E. 1992, Gravitational Lenses (Berlin: Springer)
Schneider, P., & Wagoner, R. V. 1987, ApJ, 314, 154
Schneider, P., & Weiss, A. 1987, A&A, 171, 49
Seljak, U., & Holz, D. E. 1999, A&A, 351, L10
Spada, M., Panaitescu, A., & Mészáros, P. 2000, ApJ, 537, 824
Stanek, K. Z., Paczyński, B., & Goodman, J. 1993, ApJ, 413, L7
Tadros, H., Warren, S., & Hewett, P. 1998, NewA Rev., 42, 115
Tinney, C. G. T. 1999, in ASP Conf. Ser. 165, The Third Stromlo Symposium: The Galactic Halo, ed. B. K. Gibson, T. S. Axelrod, & M. E. Putman (San Francisco: ASP), 419
Trimble, V. 1987, ARA&A, 25, 425
Turner, E. L., Ostriker, J. P., & Gott, J. R. 1984, ApJ, 284, 1
van Paradijs, J., Kouveliotou, C., & Wijers, R. A. M. J. 2000, ARA&A, 38, 379
van Paradijs, J., et al. 1997, Nature, 386, 686
Walker, M. A. 1999, MNRAS, 306, 504
Walker, M. A., & Ireland, P. M. 1995, MNRAS, 275, L41
Wambsganss, J. 1993, ApJ, 406, 29
Wambsganss, J., Paczyński, B., & Katz, N. 1990, ApJ, 352, 407
Williams, L. L. R., & Wijers, R. A. M. J. 1997, MNRAS, 286, L11